

Numerical Modeling of Stress Corrosion Cracking in Polymers

A THESIS
SUBMITTED TO THE FACULTY OF THE GRADUATE SCHOOL
OF THE UNIVERSITY OF MINNESOTA
BY

Hanxiao Ge

IN PARTIAL FULFILLMENT OF THE REQUIREMENTS
FOR THE DEGREE OF
DOCTOR OF PHILOSOPHY

Professor, Susan C. Mantell, Jialiang Le, Advisers

December, 2015

©Hanxiao Ge December 2015

Acknowledgements

I would like to express my gratitude to my advisors, Prof. Susan Mantell and Prof. Jialiang Le, for providing their invaluable insight and guiding me through this journey in the past four years. In addition, I would like to thank Dr. Haiyan Li from Dassault Systemes for sharing her knowledge on finite element analysis and fracture mechanics.

This work was support in part by grants from the National Renewable Energy Lab and the National Science Foundation.

Abstract

Polymeric materials have been increasingly used for structural purposes in civil infrastructures. However, stress corrosion cracking has been a critical issue that affects the service lifetime of polymer components. My preliminary study showed that polyethylene may be severely corroded in an oxidizing environment and lose its fracture resistance property. Experimental methods have been primarily adopted to investigate stress corrosion cracking in polymers; however, these approaches are expensive to apply, and may fail to account for certain aspects of this chemo-mechanical process. Therefore, a numerical approach is needed to investigate this issue.

A unified chemo-mechanical model is developed to predict the stress corrosion cracking (SCC) of a viscoplastic polymer. This model is applied to the specific case of high density polyethylene (HDPE) exposed to a chlorinated environment at a constant stress load. This chemo-mechanical model is comprised of three components, each capturing a critical aspect of SCC. An elastic-viscoplastic constitutive model is adopted to predict the time-dependent creep behavior of HDPE, and the model parameters have been calibrated through tensile testing. This constitutive model has been implemented in finite element analysis by using a user-defined material subroutine. The polymer fracture property is considered to be dependent on the extent of corrosion, and this dependence is implemented with a cohesive zone model. A chemical kinetics and diffusion model is utilized to predict the degradation of fracture properties in the material as a result of reactions and migration of chemical substances. The coupled chemo-mechanical simulation is accomplished by integrating the chemical reaction calculation into finite element analysis via user defined subroutines.

Two modes are considered for failure of the polymer: excessive plastic deformation or catastrophic unstable crack growth. At high stresses, the failure is primarily due to excessive plastic deformation. At low stresses, chemical reactions and diffusion are the dominant factors leading to failure. In addition, two distinct patterns of crack growth (reaction-driven or diffusion-driven) are revealed at various disinfectant concentrations at low stress levels. In reaction-driven crack growth, material degradation is localized at the crack tip, and crack growth rate is a constant throughout the simulated lifetime. However, when

diffusion dominates, the entire specimen ligament may be severely degraded, and crack growth accelerates at the end of component lifetime.

The current simulation framework allows exploring the interaction of various factors in stress corrosion cracking, such as disinfectant concentration, loading, and temperature. The framework is also general enough to be implemented for other polymeric materials and corresponding corrosion mechanisms. In the future, the proposed chemo-mechanical modeling approach may be expanded to analyze the performance of a variety of materials under stress corrosion cracking. In addition, a stochastic methodology may be incorporated to account for the variances in loading, as well as material properties.

Contents

List of Tables	vi
List of Figures	vii
Nomenclature	ix
1 Introduction	1
1.1 Motivation	1
1.2 Research objectives	2
1.3 Outline of thesis	3
2 Background	4
3 Preliminary study of the effects of environment on polyethylene fracture	8
3.1 Background	8
3.2 Experimental procedure	12
3.2.1 Sample preparation	13
3.2.2 Testing method	15
3.3 Results and discussion	16
3.4 Summary	18
4 Chemo-mechanical model for time-dependent crack growth	20
4.1 Bulk constitutive model	21
4.2 Cohesive zone model	24

4.3	Chemical reactions and diffusion model	29
4.4	Molecular weight dependence of CZM	31
5	Determination of model parameters	35
5.1	Viscoplastic constitutive model	35
5.1.1	Determination of viscoplastic model parameters	36
5.1.2	Simulation of strain history during creep loading	39
5.2	Cohesive zone model parameters for HDPE	41
5.3	Chemical reaction and diffusion constants	43
6	Numerical implementation and case study	46
6.1	Finite element analysis implementation	47
6.2	Simulation of monotonic loading	48
6.3	Simulation of stress corrosion cracking	49
7	Results and discussion	53
7.1	Monotonic load on undegraded DEN specimens	53
7.2	Constant load on SEN specimens in a chlorinated environment	58
8	Conclusions and future work	69
	Bibliography	72
	Appendix A Viscoplastic model implementation in Abaqus	78
	Appendix B Chemical kinetics and diffusion	80
B.1	Reaction and diffusion equations	80
B.2	Matlab simulation code	83

List of Tables

5.1	Viscoplastic constitutive model parameters at $20^{\circ}C$	38
5.2	Rate constants at $20^{\circ}C$ for kinetic modeling. Unit= $L/(mol \times s)$	45
5.3	Coefficients of diffusion at $20^{\circ}C$ for kinetic modeling. Unit= m^2/s	45
5.4	Yield ratios at $20^{\circ}C$	45
A.1	Algorithm for the elastic-viscoplastic constitutive model	79

List of Figures

3.1	Crack propagation in a thin film loaded in stress. r_p represents the plastic zone at the crack tip.	9
3.2	The total fracture energy is the total work done during tensile testing of a SEN specimen.	11
3.3	The essential work will decrease with increasing extent of degradation ($D1 < D2 < D3$).	12
3.4	Strain at failure data for polyethylene samples as a function of the carbonyl index.	14
3.5	Plaque sample with initial crack and ligament length L.	14
3.6	Crack propagation experimental setup, taken from [46]	15
3.7	Crack growth in moderately degraded (CI=23) and highly degraded (CI=52) SEN polyethylene samples	17
3.8	Carbonyl Index plotted against w_T . The uncertainty in the essential work is a result of variability in the ligament length.	18
4.1	Schematic representation of the cohesive zone and traction separation relation	26
4.2	A bilinear traction separation curve	27
4.3	The definition of damage parameter ω'	29
4.4	Model of a semicrystalline polymer	31
4.5	The characteristic length as a function of molecular weight	33
5.1	Deformation of a dogbone specimen during tensile testing	37
5.2	True stress and strain relations of HDPE at various strain rates	39

5.3	The creep testing apparatus	40
5.4	The strain history of dogbone specimens under creep	41
5.5	Nominal section strength as a function of L (plotted using data from [35])	42
5.6	Molecular weight dependence of τ_{max} and G_{Ic}	44
6.1	DEN and SEN specimens in finite element analysis	48
6.2	Algorithm for implementing coupled simulation of mechanical and chemical kinetics models	51
7.1	Load displacement curves for specimens of various ligament lengths. Ligament=4mm is used to calibrate G_{Ic}^0	54
7.2	Simulated load displacement curves with various sizes of cohesive element	56
7.3	Simulated load displacement curves with various mesh densities through the specimen thickness	56
7.4	57
7.5	Crack growth history when stress=1.11MPa	59
7.6	Crack growth rate versus stress intensity factor for two distinct sets	60
7.7	Molecular weight profile for (a) 0.15ppm and (b) 0.0005ppm, at three crack lengths respectively	62
7.8	M_w profiles for [DOC]=0.0005ppm at $K=10MPa \cdot \sqrt{mm}$	63
7.9	Characteristic times of diffusion and reaction for (a) 0.15ppm and (b) 0.0005ppm	64
7.10	Simulated lifetime-stress relations for (a) 0.15ppm and (b) 0.0005ppm at 20°C	66

Nomenclature

\bar{x}, \bar{s}	number of crosslinking and chain scission
β	relative thickness parameter
δ_c	separation displacement at failure
$\dot{\Delta}$	load point displacement rate
$\dot{\epsilon}^p$	uniaxial plastic strain rate
ϵ_{max}	maximum strain
ω	scalar damage parameter
σ	uniaxial stress
σ_{nom}	Nominal section stress
τ_{ch}^R, τ_{ch}^D	characteristic times for reaction and diffusion
τ_{max}	maximum traction
a, a_0	crack length, initial crack length
D_{O_2}, D_{DOC}, D_{AO}	diffusion coefficient
$E, C, n, \beta, \gamma, d_{1,2,3}, X_0, \nu$	Viscoplastic model constants
F	load
G_{Ic}	fracture toughness
H, W	specimen height and width

K	stress intensity factor
k	rate constants for chemical kinetics model
L	ligament length
l_{ch}	characteristic length
m	power constant
M_w, M_c	weight average molecular weight, threshold molecular weight
T	specimen thickness
t	time
T_g	glass transition temperature
X	hardening state variable
x	location in a 1D space
ABS	Acrylonitrile Butadiene Styrene
AO	anti-oxidant
BC	boundary condition
CCG	creep crack growth
CZM	cohesive zone model
DEN	double edge notch
DOC	chlorine dioxide
FEA	finite element analysis
HDPE	high density polyethylene
HE	hydrogen embrittlement
IC	initial condition
PE	polyethylene

PEX cross-linked polyethylene

PMMA poly(methyl methacrylate)

PVC polyvinyl chloride

SCC stress corrosion cracking

SEN single edge notch

Chapter 1

Introduction

1.1 Motivation

Polymeric materials have become increasingly popular in structural applications because of their superior corrosion resistance and lighter weight compared with metals. Specifically, commodity plastics have been widely adopted for civil infrastructure due to low cost. For instance, polyethylene and polyvinyl chloride (PVC) are used to build geomembranes, which serve to control the migration of fluids. Polyethylene pipes are primarily implemented in natural gas distribution systems and account for more than 90% of usage in North America [21]. For potable water transportation, the piping products are commonly made of polyethylene, PVC, cross-linked polyethylene (PEX), and Acrylonitrile Butadiene Styrene (ABS). In a recent market survey, it was pointed out that the total US demand for plastic pipes would increase from \$7.5B in 2010 to over \$11B in 2015 [24]. The polymeric geomembrane market worldwide is estimated to be \$3.4B in 2019, doubling that in 2013 [41]. The tremendous surge in demand for plastic pipelines arises from both new construction and replacement of retired water/gas delivery systems.

Longevity and structural integrity of polymeric components in these infrastructure applications are of particular concern to designers. For example, geomembranes have been widely used to contain hazardous and waste liquid/solid. Disinfectants (oxidizers) in potable

water can severely degrade the inner surface of plastic pipelines, causing significant crack formation and eventually a complete failure. Service times of failed water pipes vary between 1 to 25 years, significantly lower than the expected lifespan of 50 to 100 years [19]. Published data for these applications have confirmed that the interaction between stresses and environment could accelerate the polymer degradation and lead to crack formation and propagation, referred to as stress corrosion cracking (SCC).

To design structural components that satisfy the lifetime requirements, the coupled effects of stress and chemical induced corrosion should be properly understood. This will enable an accurate evaluation of polymer failure due to SCC.

1.2 Research objectives

The objective of this study is to construct a numerical model to simulate the time-dependent failure of polymers under SCC. Specifically, the case of HDPE exposed to a chlorinated environment is explored. Degradation of HDPE involves the reactions and diffusion of multiple reactants, including disinfectants, antioxidants and the polymer structure. This reaction-diffusion process is simulated with a kinetics model, and integrated into a mechanical analysis. The HDPE fracture property is considered to be dependent on the extent of corrosion, and such dependence is implemented with a cohesive zone model. Meanwhile, the nonlinear time-dependent stress strain relations of HDPE are characterized through a viscoplastic constitutive model.

A case study is performed to investigate the performance of an HDPE specimen in a chlorinated environment and under stress. This scenario is representative of a polymer pipe used in water distribution. Failure of the HDPE specimen at various disinfectant concentrations and stresses is evaluated and discussed.

1.3 Outline of thesis

Chapter 2 gives an overview of the existing literature on stress corrosion cracking in polymers.

Chapter 3 presents a preliminary study on the fracture mechanics performance of degraded polyethylene thin films.

Chapter 4 proposes a chemo-mechanical modeling approach that can be used to simulate SCC in a viscoplastic polymer.

Chapter 5 describes the calibration of material model parameters based on experimental study and existing literature.

Chapter 6 develops a methodology to apply the chemo-mechanical modeling using a co-simulation approach, and its implementation via finite element analysis.

Chapter 7 presents the results of FEA simulations, with an emphasis on the case study of an HDPE specimen exposed to a chlorinated environment. Specifically, the crack growth history and the ultimate failure mechanisms are explored.

Chapter 8 summarizes the chemo-mechanical model and its application in the SCC of HDPE. Recommendations for future work are also provided.

Chapter 2

Background

For polymers, creep crack growth (CCG) describes the slow crack propagation induced by the material viscoplastic behavior. CCG occurs at a stress level that is significantly lower than the material yield stress, and the fracture mode is brittle. Typically, SCC involves two aspects of failure: mechanical failure due to CCG, and chemical induced material degradation.

The research regarding CCG and SCC has been primarily empirical: field failure data were reported [11, 20], controlled experimental studies have been conducted on samples that have been degraded in the field or laboratory [28], and accelerated aging methods have been developed to elicit failure in a short time [9, 16, 36]. Test standards for specific applications have been developed: For example, ASTM D1693 [12] and F2136 [23] describe test procedures for polyethylene pipes exposed to chlorinated water (an oxidative environment), and ASTM D5397 [13] and D5747 [14] describe procedures for evaluating the performance of polyolefin geomembranes.

Due to the long service time of structural polymer components, accelerated testing has been broadly used to study both CCG and SCC. For instance, Lu et al. [38] conducted extensive tests at elevated temperature to study the CCG of a polyethylene copolymer. In these tests, single edge notched (SEN) tensile specimens were subjected to a constant stress load. The geometry of the SEN specimens was designed so that a plane strain condition

would occur. The tests were performed at various temperatures (from room temperature to 80°C) and different stress levels. Two failure modes were observed: ductile failure due to large deformation at high stresses, and brittle failure due to CCG at low stresses. Specimen lifetime was obtained as a function of stress level for each temperature. A unifying equation was developed to relate the lifetime-stress relations at various temperatures: lifetime at room temperature can therefore be extrapolated from the higher temperature data. The accelerated testing method has been widely adopted by other researchers to study CCG[36].

In the study of SCC, accelerated testing of polymers typically involves the use of high reactant concentration in addition to high temperature. Hsuan et al. [29] developed a Notched Constant Tensile Load test to evaluate the stress corrosion resistance of high density polyethylene geomembranes. In this test, SEN tensile test specimens were immersed in a highly corrosive environment (10% Igepal) at an elevated temperature when constant tensile stresses are applied. The ultimate specimen failure time, as well as the applied stress, revealed the resistance of the tested resin to SCC. Dear et al. [16] conducted experiments on water pipes that were made of medium density polyethylene (MDPE). The pipes were pressurized to provide a hoop stress up to 4.6MPa at 80°C . The chlorine concentration used for testing varied between 500 and 120000 mg/L. Experimental data showed that in a high concentration chlorine solution at high temperature, only brittle failure occurred, regardless of the stress level. The pipe lifetime was reduced with increasing concentration. The inner surface of pipes was severely embrittled due to chemical reactions and diffusion.

The accelerated testing method is a valuable tool to measure the polymer performance under CCG and SCC, at least on a comparative basis. For instance, pipe manufacturers can use this approach to select the best performing material among multiple candidates. However, using this approach to predict the polymer behavior at low temperature/reactant concentration via extrapolation has some flaws. Lang et al. [36] pointed out that structural changes in a material due to temperature variations and thermal/chemical aging may compromise, even invalidate the predictions made by this approach. For example, in the accelerated aging treatment of polyethylene, stability of the free chlorine components de-

depends on the temperature. Devilliers et al. [17] argued that both hypochlorous acid (HClO) and the hypochlorite (OCl) ion become unstable when temperature is higher than 40°C . Therefore, the degradation mechanism in a chlorinated environment at high temperature may be different from that under room temperature. Using the accelerated testing results to extrapolate for normal service conditions could lead to inaccuracies for this reason.

By contrast, numerical simulation provides a flexible means that enables the prediction of polymeric component lifetime. Performance of different materials and part geometries during the entire lifetime can be conveniently evaluated using finite element analysis (FEA). In addition, the coupling effects of multi-physics (thermal, mechanical, chemical, etc.) can be readily evaluated, which is usually impractical if pursued experimentally. Therefore, numerical simulation is a promising method for the accurate predictions of polymer lifetime under SCC.

FEA has been utilized for the prediction of PE failure under CCG. Hutar et al. [31] developed a simulation approach to estimate the lifetime of pressurized HDPE pipe. Power law crack growth kinetics were extracted from a compact tension specimen under static loading at 80°C . This kinetics relationship was used to obtain the total failure time for a particular crack growth history. The stress intensity factor at various crack lengths was evaluated from FEA calculations. However, this method cannot be easily implemented at lower temperatures due to the difficulties in acquiring the kinetics relationship.

In order to predict failure under SCC, a chemical kinetics simulation must be coupled with the mechanics model. Choi et al. [5] developed a numerical simulation scheme of SCC in a thermoplastic material based on crack layer theory. In this study, SCC is considered a superposition of creep induced aging and chemical degradation. The loss of material toughness due to these two mechanisms was characterized via phenomenological power laws. A generic kinetic parameter was proposed to represent the rate of chemical corrosion. Both SCC and mechanically driven crack growth were simulated. The parametric approach in this study effectively reveals the similarities and differences between SCC and CCG.

However, one of the features of SCC is that it strongly depends on the diffusion process,

and the migration of substances is critical to the corrosion of a structure. Olden et al. [42] constructed a numerical method to study the effects of hydrogen embrittlement (HE) on steel property. HE is a diffusion driven mechanism that significantly corrodes steel. Hydrogen slowly diffuses into the process zone around the crack tip and accumulates there, resulting in reduction of material strength and toughness. In this study, the diffusion of hydrogen was incorporated in the finite element simulation, and the extent of degradation was predicted as a function of hydrogen concentration. A cohesive zone model was utilized to characterize the nonlinear fracture property and its variation with hydrogen concentration.

The methods provided by Choi et al. and Olden et al. are promising tools to predict SCC of a structure. However, diffusion controlled degradation of polymers poses additional challenges that must be addressed. For polymers, disinfectants and oxygen from the environment diffuse into the structure and react with the material in an oxidation-reduction process. Antioxidants are commonly added to retard the reactions by neutralizing the oxidizers. To investigate SCC in a polymer, the oxidation reactions must be simulated in situ with the fracture analysis. In addition, the diffusion of *multiple reacting substances*, including both oxidizers and antioxidants, should be predicted. This motivates the development of a unified computational model that takes into account the interactions between chemical reactions, diffusion, and mechanical deformation.

Chapter 3

Preliminary study of the effects of environment on polyethylene fracture

The objective of this preliminary study is to demonstrate the effect of environmentally induced degradation on the fracture property of PE. Specifically, thin film specimens were exposed to accelerated aging conditions to obtain various extents of degradation. Applications that involve the use of PE films for structural purposes include solar collectors and geomembranes. In these scenarios, the material can be oxidized due to its exposure to UV light and corrosive species from the surrounding liquid environment. In addition, the use of thin specimens during accelerated aging is critical to achieve uniform degradation through the thickness. The relationship between fracture property and degradation can be properly investigated.

3.1 Background

The resistance of thin polymer films to crack growth will significantly impact the lifetime. Fracture toughness is a property that describes the capacity of a material to resist brittle

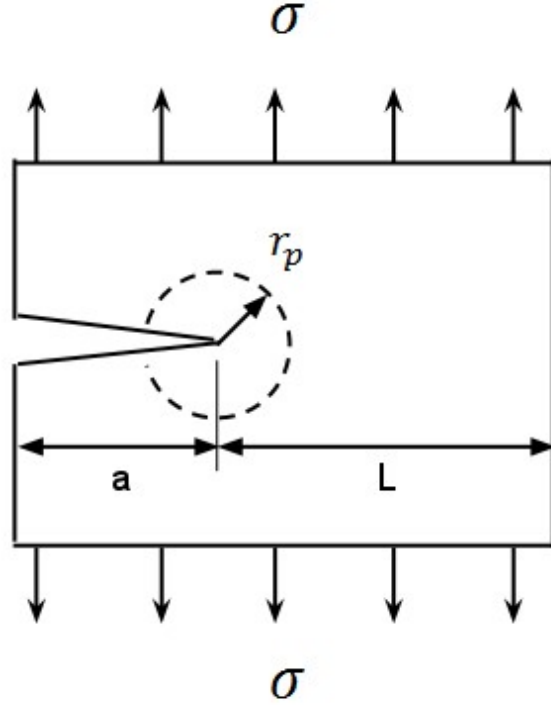


Figure 3.1: Crack propagation in a thin film loaded in stress. r_p represents the plastic zone at the crack tip.

crack growth. A material with higher fracture toughness is more resistant to crack initiation. This property is very important in engineering design and can be expressed in terms of the critical stress intensity factor K_c . For a film subjected to a tensile stress σ with an initial crack length a (see Fig 3.1), the stress within the film must be less than the critical stress σ_c that causes crack propagation:

$$\sigma < \sigma_c \quad \text{where} \quad \sigma_c = \frac{K_c}{F(a/W)\sqrt{\pi a}} \quad (3.1)$$

The critical stress is defined in terms of K_c , the geometry factor F (a function of the initial crack length and width W) and the initial crack length a . While K_c has been characterized for many polymer films [1], the property has not been characterized for degraded polymer films or as a function of the extent of the film degradation. In general, polymer materials are often subjected to conditions that cause degradation throughout their lifetime. Thus, a method to evaluate K_c as a function of the extent of degradation is important to designing

a polymeric components.

In selecting a method for evaluating K_c , the film must be classified as either loaded in plane strain or plane stress. In general, plane stress is assumed for thin films while bulk 'plate-like' samples are characterized as plane strain. In the present study, the film thickness is such that plane stress loading conditions apply. There are several established test procedures for evaluating K_c for plane stress conditions. Crack propagation in the film will also depend on whether the material failure is brittle or ductile.

The residual strength analysis method, proposed by Klemann [32], is applicable for brittle polymer films. This method is based on the theory of Linear Elastic Fracture Mechanics (LEFM). The method entails testing of single edge notch (SEN) samples with varying initial crack lengths. The stress at rapid crack growth is recorded. The stress data are curve fit to an equation of the form Eqn 3.1 to find the critical stress intensity factor K_c .

The essential work method (EWM) has been applied to evaluate fracture toughness (and K_c) of ductile materials. In the essential work method [4, 39, 44], the work required to fracture SEN samples loaded in tension is evaluated. The total work in fracture W_T is attributed to two sources: the essential work W_e that results in tearing and forming a necked region, and the non-essential work W_p expended in plastic deformation of the outer region. While there is also energy dissipation due to the viscoelastic nature of the polymer film, this work is considered small compared to W_e and W_p and therefore negligible. The specific fracture energy w_T is further defined as the total work W_T divided by the ligament efficiency, which is defined as the product of the ligament length L and sample thickness T .

$$w_T = \frac{W_T}{L \cdot T} \quad (3.2)$$

Thus, the specific fracture energy is approximated as [3]:

$$w_T = w_e + \beta w_p L \quad (3.3)$$

where β is a proportionality constant related to the non essential work. Eqn 3.3 describes the linear relationship between the total specific energy of fracture and the ligament

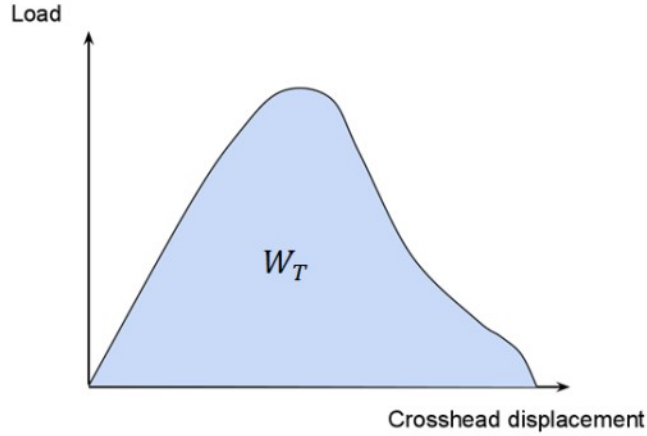


Figure 3.2: The total fracture energy is the total work done during tensile testing of a SEN specimen.

length.

The critical stress intensity factor can be determined from the specific essential work we as follows. Mai et al. [39] showed that w_e is equivalent to the critical J integral J_c . The J integral, for the case of small scale yielding, is related to the stress intensity factor K:

$$J = \frac{K^2}{E} \quad (3.4)$$

where E is the elastic modulus. Thus, for the critical condition (at which the crack begins to propagate), K_c can be found from the essential work of fracture [44]

$$w_e = \frac{K_c^2}{E} \quad (3.5)$$

To implement the essential work method, rectangular samples with a single edge notched are prepared. Sample geometry restrictions have been proposed by Hashemi [27]. The SEN samples are loaded in tension at a constant rate and the load as a function of crosshead displacement is recorded. The total fracture energy W_T is calculated by integrating the load over the crosshead displacement (Fig 3.2). Then, the specific fracture energy w_T is evaluated by dividing the total energy by the ligament efficiency. The data are plotted as a function of the ligament length and fitted with a line (see Eqn 3.3). The resulting intercept

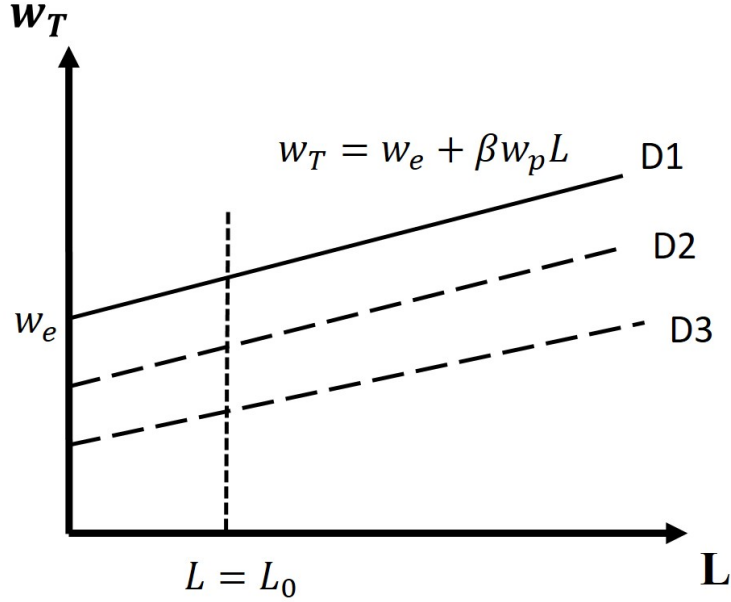


Figure 3.3: The essential work will decrease with increasing extent of degradation ($D1 < D2 < D3$).

with the $L=0$ axis is the specific essential fracture work w_e (see Fig 3.3). It is anticipated that as the extent of degradation progresses the essential fracture work will decrease, as shown in Fig 3.3.

Regardless of the test method, residual strength analysis or the essential work method, many samples, each with a different ligament length, are required to determine K_c . In order to determine K_c as a function of degradation, the test must be repeated not only over a range of ligament lengths but also for several degradation levels.

3.2 Experimental procedure

The experimental procedure can be summarized as follows:

- Thin film samples are degraded through exposure to hot chlorinated water.
- The extent of degradation of each sample is characterized by the carbonyl index.
- A screening test is performed to determine whether a brittle or ductile test method for determining K_c is applicable.

- A pilot study to evaluate the effect of the extent of degradation on crack propagation is performed.

The polyethylene samples used in the present study exhibited ductile failure over the entire range of degradation. Thus the sample and procedures outlined in the following sections correspond to the guidelines for evaluating K_c through the essential work method.

3.2.1 Sample preparation

The MDPE specimens used in this experiment is prepared by compression molding. The material is compounded with phenolic antioxidant. The undegraded material has a density of $0.936g/cm^3$, and a molecular weight $M_w = 200kg/mol$. Thin MDPE film plaque samples are exposed to $80^\circ C$ chlorinated water for up to 45 days. The plaque sample dimensions are 32 mm by 44 mm by 0.3 mm thick. The water bath conditions are controlled such that the concentration of the chlorine is maintained at 8ppm and the pH is 6.8 ± 0.2 . The ORP (oxidation reduction potential) is in the range of 700 - 750 mV. The extent of degradation in these samples is characterized by Fourier Transform Infrared Spectroscopy (FTIR). These researchers showed that there is a correlation between the carbonyl index and the material strain at failure (Fig 3.4). In this case the carbonyl index is defined as the ratio of the area of the OX band ($1690 - 1790cm^{-1}$) to the peak corresponding to polyethylene ($2018cm^{-1}$). The carbonyl index for unexposed (not degraded) samples is less than 10. The carbonyl index for samples with the longest exposure time is greater than 50. By using FTIR, the extent of degradation of a sample can be characterized nondestructively, prior to evaluation of the fracture toughness. Moreover, because the samples are thin films, the extent of degradation can be assumed to be uniform through the thickness of the sample [50].

Exposed samples were removed from the bath at intervals ranging from days to week in order to achieve a range of degradation levels. The carbonyl index for each sample was measured by FTIR. For the fracture toughness experiments, SEN specimens were prepared by introducing an initial crack in the (degraded) plaque samples using an X-ACTO knife (Fig 3.5). The crack length was set such that the ligament length L was $5.1 \pm 0.6mm$.

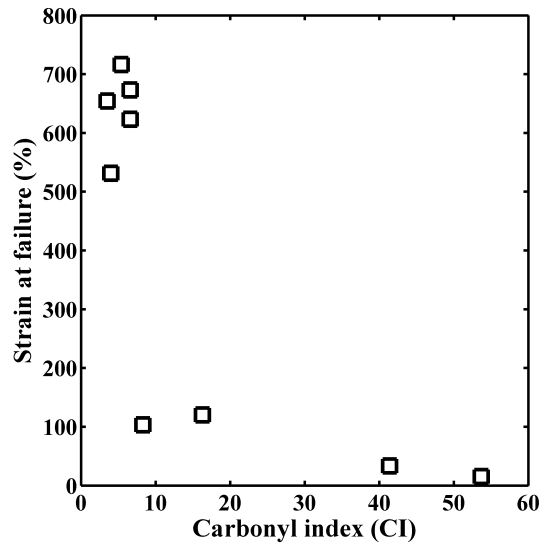


Figure 3.4: Strain at failure data for polyethylene samples as a function of the carbonyl index.

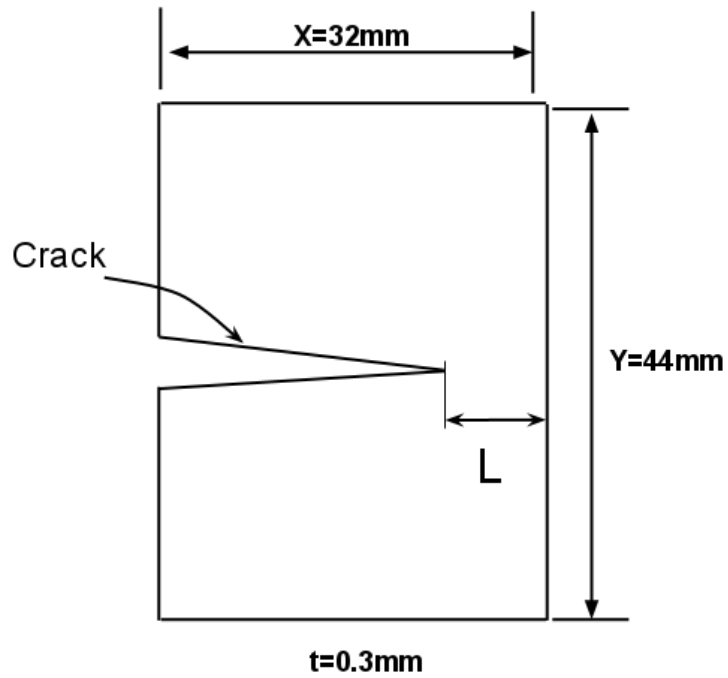


Figure 3.5: Plaque sample with initial crack and ligament length L .

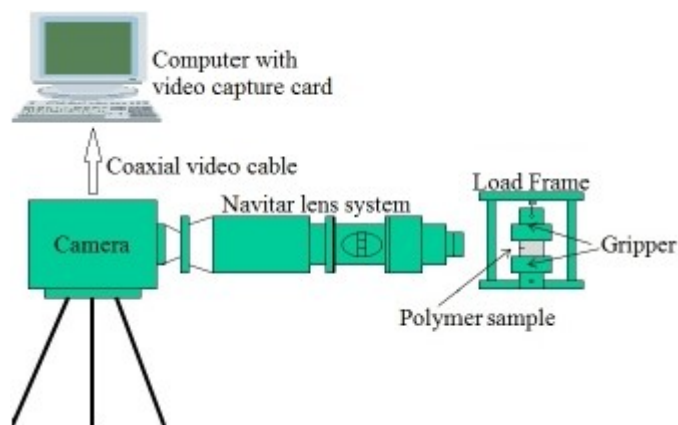


Figure 3.6: Crack propagation experimental setup, taken from [46]

3.2.2 Testing method

Tensile test samples (for characterization of ductile/brittle failure) or SEN samples are loaded on an MTS QTest machine. During SEN tests, crack initiation and growth are recorded by a digital camera and a video capture card. The video recording apparatus consists of a Panasonic CCTV camera(WV-BP330), Navitar lens system, a tripod stand, a video capture card (HD 600 PCI Digital and Analog TV Tuner from ATI TV wonder), and a computer with video editing and processing software. Fig 3.6 is a schematic illustration of the experimental setup.

The ductility of the degraded film samples can either be determined by measuring the strain at failure during a tensile test or observing the fracture propagation around the crack tip of a SEN specimen loaded in tension. If the strain at failure is less than 1% [1, 507] or the region near the crack tip shows no yielding, then the film is brittle. In the present study, both approaches were used.

The extent of degradation in degraded plaque samples was characterized by evaluating the carbonyl index using FTIR data. Based on the carbonyl index, samples are selected to span a range of degradation levels. From this group of samples that represent a range of degradation levels, SEN samples were prepared at a single ligament length, $5.1 \pm 0.6mm$ (Fig 3.5). The SEN samples were loaded in tension at a constant displacement rate. Load vs. displacement data, and video images of crack initiation/propagation were recorded

throughout the test. The specific fracture energy is calculated following the procedure as previously described.

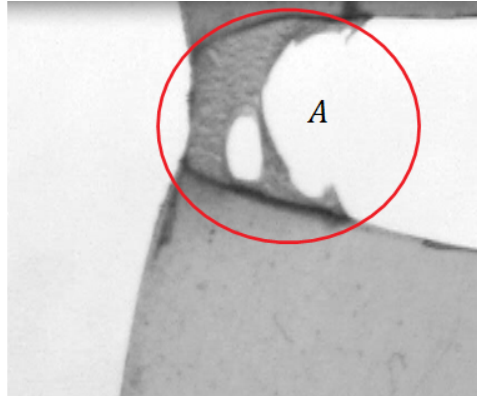
3.3 Results and discussion

The carbonyl index data for degraded plaque samples used in this study ranged from 10 to 90. A high carbonyl index corresponds to a more degraded sample. Strain at failure data for polyethylene plaque samples with similar carbonyl index values were published in [46] (see Fig 3.4). For less degraded samples, with a carbonyl index < 10 , the strain at failure can be as great as 700%. As the material degradation increases, to a carbonyl index greater than 50, the strain at failure asymptotically approaches 15%. Even at this highly degraded state, the sample strain at failure behavior is considered ductile. These published data were used to infer that the material failure behavior for the samples used in the present study is ductile.

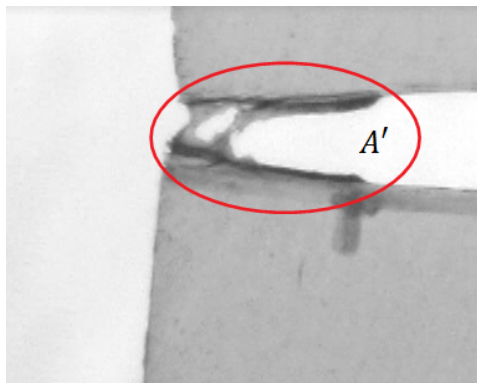
Since the sample ductility is related to the extent of degradation, the material ductility can be determined with FTIR without destroying the sample. Therefore, FTIR analysis is an alternative and nondestructive measure of the strain at failure.

Data from video images recorded during testing of SEN samples further confirm that the degraded film exhibited ductile behavior. Figure 3.7a and fig 3.7b show video images of crack growth in moderately degraded (CI=23) and highly degraded (CI=52) SEN specimens. Zone A and zone A' indicate the corresponding plastic deformation areas on the two samples. It can be observed that plastic deformation is much greater in the less degraded sample, indicating higher material ductility. For the highly degraded sample, some traces of ductile failure can still be observed, although in a less significant manner. In both cases, the surface of the fracture is fibrous, and voids grow in the vicinity of the crack tip. These are all typical characteristics of ductile fracture.

The work of fracture w_T was evaluated for ten samples, each with a ligament length of $5.1 \pm 0.6mm$. The error in w_T is caused by the variance in ligament length. Absolute error



(a) CI=23



(b) CI=52

Figure 3.7: Crack growth in moderately degraded (CI=23) and highly degraded (CI=52) SEN polyethylene samples

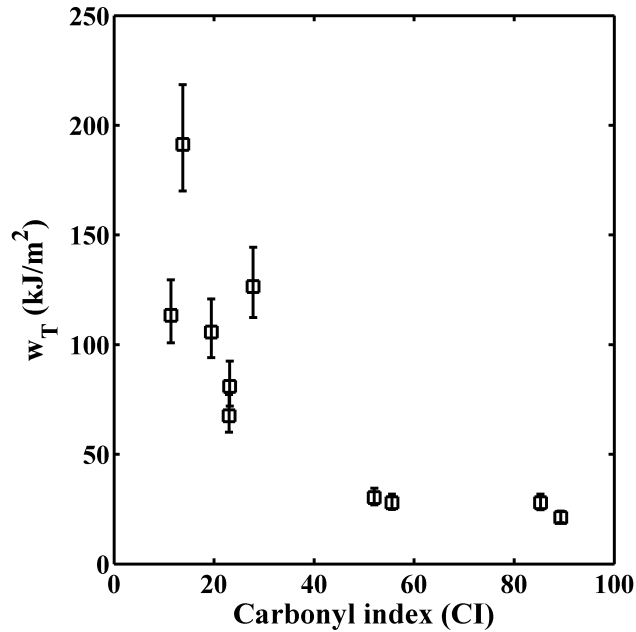


Figure 3.8: Carbonyl Index plotted against w_T . The uncertainty in the essential work is a result of variability in the ligament length.

decreases with increasing degradation, but relative error remains almost constant (about 25%) for all specimens. For carbonyl index less than 30, w_T ranged from $70 - 180 \text{ kJ/m}^2$ (Fig 3.8). As sample degradation increases (increasing carbonyl index), the specific work of fracture decreases. This trend is reasonable since it is expected that as the material becomes more brittle, the fracture toughness will decrease. The specific work of fracture w_T approaches a threshold value of approximately 25 kJ/m^2 for samples with a carbonyl index of 50 or greater.

3.4 Summary

A preliminary study has been developed to evaluate the effect of degradation on crack propagation in thin polyethylene films. Thin film samples were degraded in an oxidative environment (chlorinated water) at an elevated temperature for up to 45 days. The extent of degradation is quantified by evaluation of the carbonyl index. Data are also presented which show a close correlation between carbonyl index and strain at failure: strain at failure

decreases as the polyethylene becomes more degraded. Because the polyethylene, even in a degraded state, exhibits ductile fracture behavior, an essential work method is proposed to quantify the fracture energy of the film.

The fracture testing data are limited to a single ligament length $L_0 = 5.1mm$, but span a range of material degradation levels. This study, then, represents the case of a vertical line at $L = L_0$ through several sets of essential work data each at a single level of degradation (see Fig 3.3). The effect of degradation on the critical stress intensity factor can be quantified by studying crack initiation and propagation over a range of ligament lengths.

This preliminary study demonstrates the diminished fracture performance of polymers that have been degraded. Thus, it is desirable to develop a model that can account for the effects of degradation of material property, as well as predict crack growth in degraded materials.

Chapter 4

Chemo-mechanical model for time-dependent crack growth

In this chapter, a generic chemo-mechanical model is proposed to simulate time-dependent crack growth in polymers. Specifically, it is developed to study SCC of HDPE. The chemo-mechanical model consists of three sub-models, each capturing a critical aspect of SCC. An elastic-viscoplastic constitutive model is adopted to characterize the nonlinear time-dependent behavior of HDPE. The material fracture property is considered to be dependent on the extent of corrosion, and this dependence is implemented with a cohesive zone model. A chemical kinetics and diffusion model is utilized to predict the degradation of fracture properties as a result of reactions and migration of chemical substances, and multiple reactants are considered. Implementation of the chemo-mechanical model involves finite element analysis in Abaqus, and chemical kinetics simulation in Matlab. User subroutines are utilized to connect the data flow between these two simulation platforms.

The chemo-mechanical model is developed in a general form that is readily applicable to other viscoplastic polymers in addition to HDPE.

4.1 Bulk constitutive model

The mechanical behavior of HDPE is highly nonlinear: the constitutive law is a function of strain history, loading rate, and also temperature. For instance, creep causes both ductile and brittle failure in HDPE pipes ([26], [33]) at room temperature. Creep occurs at a stress much lower than the material yield stress; therefore this behavior cannot be estimated using an elastic material model. It is also well known that the stress-strain behavior of polyethylene is highly sensitive to the loading rate. To simulate the mechanics of PE, some criteria must be considered to properly select a constitutive model:

- The model should be able to characterize a nonlinear time-dependent stress-strain relationship
- Model parameters must be determined through common mechanical testing approaches
- The model formulation should be adaptable in finite element analysis
- Ideally, the model has been validated for PE under large deformation (i.e., strain greater than 10%)

Constitutive models that characterize the nonlinear stress and strain behavior have been proposed by various researchers. Despite significant differences in form, these models are all constructed from a phenomenological uniaxial stress and strain relation. Kurtz et al. ([34]) proposed an exponential model to predict the tensile true stress and strain behavior of irradiated and oxidized ultra-high molecular weight polyethylene. This is a rate-independent model in which true stress is a function of material density and strain. The model is applicable for strain up to 12%. However, due to the lack of time-dependence, this model is not able to characterize the creep behavior of PE.

Liu et al. [37] developed a nonlinear time-dependent model for PE based on the multi-Kelvin element theory and a power law function. The model was shown to give good predictions for HDPE under both step loading or creep loading for small strains. However, the model parameter calibration involves extensive creep testing at various stress levels,

which is very time-consuming. Additionally, even though this model is applicable to predict the uniaxial stress-strain relations, its implementation in a finite element analysis framework would be very difficult due to its formulation.

Colak et al. [8] proposed a viscoplastic model based on overstress. It was used to characterize the viscoelastic and viscoplastic behavior of HDPE, and successfully implemented to predict the behavior under cyclic loading and unloading, in addition to monotonic loading and creep. Drozdov et al. [18] constructed a viscoelastic-viscoplastic model for semi-crystalline polymers, and demonstrated its application in HDPE. However, these two models involve a total of 14 and 21 parameters respectively, which makes the material calibration very difficult.

Hamouda et al. [25] presented a double inelastic deformation model, which consists of two viscoplastic strain components. These two components have different strain rate sensitivities, which are intended to reflect the strain mechanisms in both the crystalline and amorphous region of a semi-crystalline polymer. Material calibration for this model involves significant testing efforts: monotonic testing, stress relaxation, and dip-testing (creep test with two consecutive stress levels) must all be utilized.

Zhang et al. [51] proposed a viscoplastic model to characterize the rate-dependent behavior of high density polyethylene in various loading conditions, including constant strain rate and creep loading. This model was constructed on the framework of Bodner's theory [3]. The underlying assumption of this theory is that plastic deformation occurs during all stages of loading. This assumption can be represented in the form of strain decomposition: total true strain ϵ is the sum of elastic strain ϵ^e and plastic strain ϵ^p .

$$\epsilon = \epsilon^e + \epsilon^p \quad (4.1)$$

In the formulation of a time-dependent constitutive relation, the strain rate is an important factor. Therefore, the strain decomposition is formulated differently:

$$\dot{\epsilon} = \dot{\epsilon}^e + \dot{\epsilon}^p \quad (4.2)$$

The upper dot indicates strain rate (time derivative). The plastic strain rate $\dot{\epsilon}^p$ is proportional to the deviatoric strain tensor σ'

$$\dot{\epsilon}^p = \lambda \sigma' \quad (4.3)$$

The second invariants of the plastic strain rate and deviatoric stress tensors are defined as

$$D_2^p = \frac{1}{2} \dot{\epsilon}^p \dot{\epsilon}^p \quad (4.4)$$

$$J_2 = \frac{1}{2} \sigma' \sigma' \quad (4.5)$$

A power law is utilized to relate the plastic strain rate with deviatoric stress

$$D_2^p = C_0^2 \left(\frac{3J_2}{X^2} \right)^n \quad (4.6)$$

where n is a material constant. C_0 is a scale factor that can be incorporated into X . In this relation, a hardening state variable X is introduced to account for the rate dependence and strain hardening effects.

$$X = X(\dot{\epsilon}^p, W^p) \quad (4.7)$$

where W^p is the plastic work:

$$W^p = \int \sigma d\epsilon^p \quad (4.8)$$

The 3D formulation of flow rule in Eqn 4.6 can be simplified for the uniaxial case as

$$\dot{\epsilon}^p = C \left(\frac{\sigma}{X} \right)^n \quad (n \geq 1) \quad (4.9)$$

In this formula, σ refers to the uniaxial stress, and $\dot{\epsilon}^p$ denotes the uniaxial plastic strain rate. C and n are material constants. In the context of strain decomposition, the uniaxial stress and strain relation is

$$\epsilon = \epsilon^p + \epsilon^e = \epsilon^p + \sigma/E \quad (4.10)$$

where E is the time-independent elastic modulus. The hardening state variable X is further defined in the following form:

$$X = \frac{X_0}{\alpha + \sqrt{\frac{\beta}{\gamma + W^p}}} \quad (4.11)$$

The parameter α is assumed to be a function of effective plastic strain rate in a general exponential form

$$\alpha = d_1 \exp(d_2 (\dot{\epsilon}^p)^{d_3}) \quad (4.12)$$

For Zhang's model, a total of 10 parameters must be calibrated, which can be conducted with monotonic testing. This constitutive model has been characterized for HDPE by Zhang et al. [51] for up to 15% of strain in compression testing. In this study, we adopted this model to simulate the time-dependent behavior of PE.

4.2 Cohesive zone model

In this study, a fracture mechanics model was selected that can characterize the unique fracture behavior of PE under stress corrosion cracking. During SCC, the material properties vary continuously as a result of chemical corrosion. Oxidation leads to shorter polymer chains, and thus a loss of fracture toughness. Furthermore, the corrosion process is assisted by the diffusion of reacting species, and the property degradation profile forms a gradient below the material surface. Additionally, the damage zone in PE involves highly nonlinear

stress and strain relations. In the case of undegraded PE, large strains may also occur due to high ductility. Therefore, the fracture model must be in a generic form that can: (1) incorporate the effects of chemical corrosion by assigning the fracture properties as a function of degradation; (2) be implemented in the entire diffusion-affected crack zone; and (3) characterize the nonlinear stress and strain relations in the damage zone.

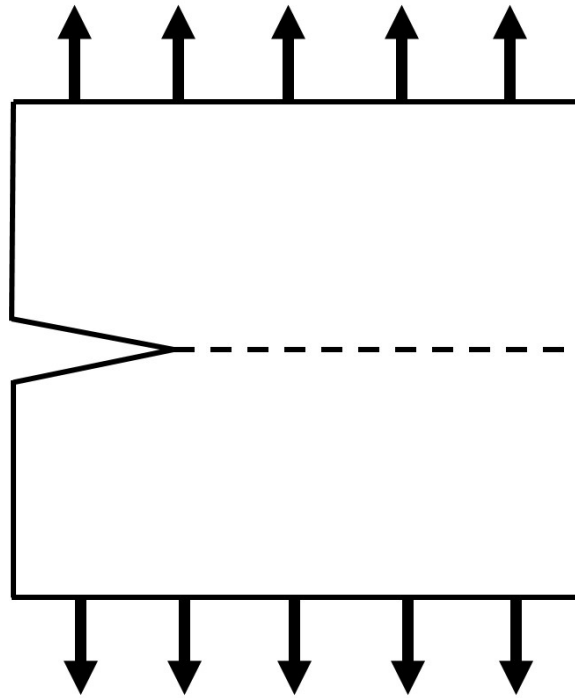
A linear elastic fracture mechanics (LEFM) approach is often used to investigate crack propagation in materials where small deformation is predominant. In this framework, the material behaves in a brittle manner such that fracture/failure occurs before yielding. Linear elasticity theory is used to compute the stress and strain field around the crack tip. When the material is ductile and significant plastic deformation occurs (like in PE), linear elasticity is no longer valid, thus LEFM cannot be used.

Cohesive zone model (CZM) is a generic form to characterize the damage in the fracture process zone. It is a phenomenological model that describes the nonlinear constitutive relation between the interfacial displacement and traction. The unique formulation of CZM allows for the simulation of both crack initiation and propagation. It has been widely applied in the characterization and simulation of both ductile and brittle materials, such as concrete ([43], [47]), metals [42], polymers ([48], [52], [22]) , adhesives [49], etc. Specifically, it has been implemented on polymers of various mechanical properties. For instance, Maiti et al. [40] constructed a CZM to simulate the fatigue crack growth in epoxy based on the bilinear traction separation form. Elices et al. [22] successfully predicted the load-displacement curves of PMMA in both compression and tensile testing modes.

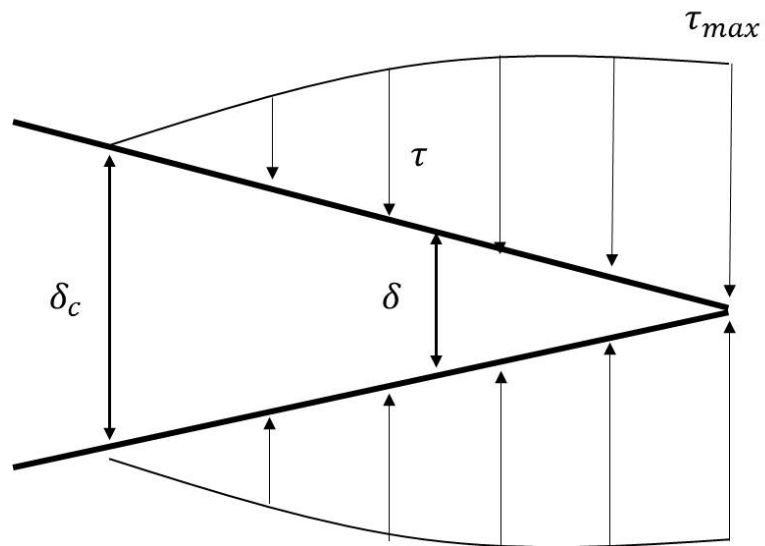
In a CZM scheme, a potential crack propagation path is predefined ahead of the crack tip (dashed line as shown in Fig 4.1a). The nonlinear constitutive relation between interfacial traction and separation displacement is illustrated in Fig 4.1b. In general, the traction is a function of separation displacement along the crack propagation path

$$\tau = \tau(\delta) \tag{4.13}$$

The crack remains closed when the traction is below the interfacial strength of the material,



(a) Cohesive zone ahead of a crack tip



(b) The interfacial traction and separation displacement

Figure 4.1: Schematic representation of the cohesive zone and traction separation relation

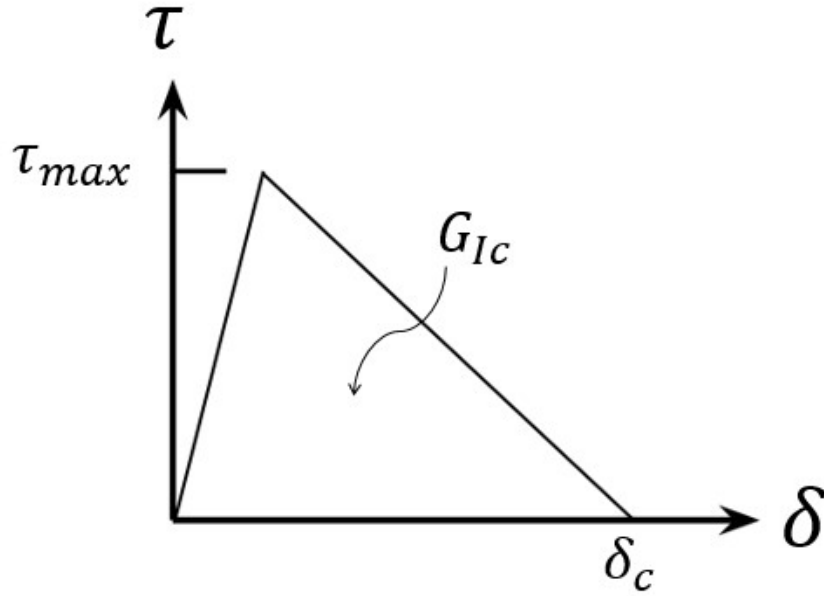


Figure 4.2: A bilinear traction separation curve

that is, the maximum stress τ_{max} . The separation displacement at the peak traction is δ_{max} . After the traction reaches its maximum value, it decreases monotonically as δ increases. This is the softening region of a traction separation ($\tau - \delta$) relation. As the traction drops to zero, the separation displacement is referred to as the displacement at failure δ_c . The fracture toughness, G_{Ic} , is calculated as

$$G_{Ic} = \int \tau d\delta \quad (4.14)$$

Various shapes have been proposed for the $\tau - \delta$ relation, such bilinear, trilinear (or bilinear softening), trapezoidal, polynomial, and exponential. Among these forms, the bilinear $\tau - \delta$ relation is the most commonly used. The shape of the bilinear traction separation curve is shown in Fig 4.2. The fracture toughness G_{Ic} is simply calculated from τ_{max} and δ_c :

$$G_{Ic} = \frac{1}{2} \tau_{max} \delta_c \quad (4.15)$$

It is noteworthy that in Eqn 4.15, any variable can be uniquely determined if two other variables are known.

The cohesive zone model can be implemented in a three dimensional space. The traction vector $\boldsymbol{\tau}$, is decomposed into a normal component (τ^n) that is perpendicular to the crack surface and two shear components (τ^s, τ^t) [15]. Similarly, the interfacial displacement is also decomposed into 3 components: δ^n , δ^s , and δ^t .

As shown in Fig 4.2, the rising part of the $\tau - \delta$ relation is defined as linear elastic. The strain of a cohesive element is defined as:

$$\epsilon_i = \delta_i / T_{coh} \quad (i = n, s, t) \quad (4.16)$$

where T_{coh} is the thickness of the cohesive layer. Linear elasticity is represented in the following format:

$$\tau_i = K_{ij} \epsilon_j \quad (i = n, s, t; j = n, s, t) \quad (4.17)$$

To simulate crack initiation, a criterion based on the nominal stress ratio is utilized. That is, the crack initiates when the maximum nominal stress ratio reaches unity:

$$\max\left\{\frac{\tau^n}{\tau_{max}^n}, \frac{\tau^s}{\tau_{max}^s}, \frac{\tau^t}{\tau_{max}^t}\right\} = 1 \quad (4.18)$$

A damage parameter ω is introduced to quantify the extent of degradation in the cohesive zone. It is a scalar variable that is between 0 and 1, and 1 indicates complete damage. ω is defined through the loss of traction due to damage:

$$\tau_i = (1 - \omega)\bar{\tau}_i \quad (i = n, s, j) \quad (4.19)$$

where $\bar{\tau}_i$ is the traction value predicted from linear elasticity if no damage existed. In a bilinear $\tau - \delta$ relation, a linear damage evolution is specified to characterize ω in terms of separation displacements:

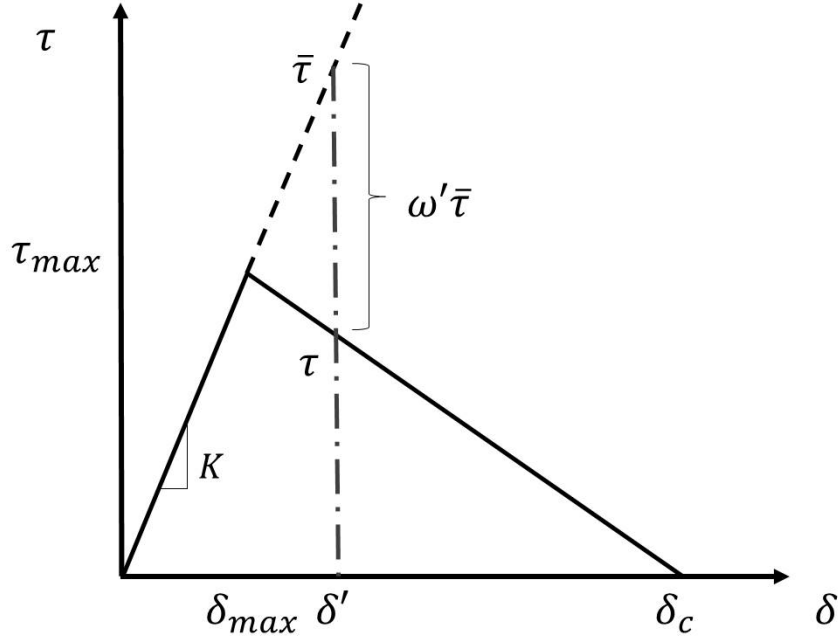


Figure 4.3: The definition of damage parameter ω'

$$\omega = \frac{\delta_c(\delta' - \delta_{max})}{\delta'(\delta_c - \delta_{max})} \quad (4.20)$$

Here, δ' is the maximum separation displacement attained through the loading history. An illustration of the damage parameter is shown in Fig 4.3.

4.3 Chemical reactions and diffusion model

In this study, we consider the case of PE exposed to chlorine as an oxidizing agent. This combination of material and environment generally occurs in PE pipes for water delivery. Antioxidants are added to PE during pipe fabrication to prevent the material from being corroded. Such antioxidants react with the oxidizing disinfectants and are slowly removed from the resin over time. Furthermore, this reaction process is accelerated by the migration of antioxidants into the surrounding liquid, as well as the penetration of disinfectants through the contact surface. After the antioxidants are depleted, PE will directly react with the disinfectants and oxygen, causing polymer chain scission and subsequently shorter molecular chains (and lower molecular weight). Both the strength and toughness of the

material will be degraded.

In a study by Colin et al. [11], a comprehensive chemical kinetics and diffusion model was developed to predict the molecular weight loss of polyethylene due to reactions with chlorine dioxide (DOC). The objective of this study was to quantitatively characterize the chemical degradation of a polyethylene pipe in a chlorinated solution. Through the simulation of chemical reactions between PE and various reactants, the molecular weight profile of PE can be determined through the pipe thickness over time. In general, the kinetics model incorporates the reactions between the following species:

- Oxygen (O_2)
- Chlorine dioxide
- Antioxidant (AO)
- Polyethylene (PE)

O_2 comes from both the chlorine solution and air. DOC is the disinfectant in this chlorinated system, and is produced by mixing hydrochloric acid (HCl) with sodium chlorite ($NaClO_2$). The antioxidant studied here is Irganox 1010. The disinfectant directly reacts with PE and produce active hydrocarbon radicals, as denoted by P° . Reactions between these radicals result in the cross linking of hydrocarbon structures, thereby increasing the molecular chain length. On the other hand, radical oxidation reactions produce hydroperoxides (POOH), which decompose and produce more hydrocarbon radicals P° and lead to molecular chain scission. The two opposing mechanisms, cross linking and chain scission, compete with each other and in conjunction determine the molecular weight of the polymer. In the early stage of polymer degradation, cross linking is the dominant reaction mechanism, while later on chain scission becomes much more significant and the molecular weight drops monotonically. The number of crosslinking \bar{x} and chain scission \bar{s} events are related to the molecular weight by:

$$\frac{1}{M_w} - \frac{1}{M_w^0} = \frac{\bar{s}}{2} - 2\bar{x} \quad (4.21)$$

where M_w^0 is the weight average molecular weight in the undegraded state, and M_w is the molecular weight after reactions initiate. The reaction and diffusion of substances are modeled in a fundamental mathematical form based on Fick's law [2]:

$$\frac{\partial[C]}{\partial t} = D \frac{\partial^2[C]}{\partial x^2} - r([C]) \quad (4.22)$$

where, $[C]$ denotes the concentration of a reactant C , and x represents the depth that C penetrates. The rate of reaction depletion r is a function of the reactant concentration. The coefficient of diffusion D is dependent on temperature. Therefore, the chemical kinetics model requires solving a set of differential equations that eventually generates the molecular weight profile in a 1D space (that is, along the direction of diffusion). The kinetic parameters (rate constant k and coefficient of diffusion D) are a function of temperature, and their values are calculated for any temperature based on the Arrhenius equation. A complete set of reaction equations are given in Appendix B.1. These equations are solved using a Matlab program, which is documented in Appendix B.2.

4.4 Molecular weight dependence of CZM

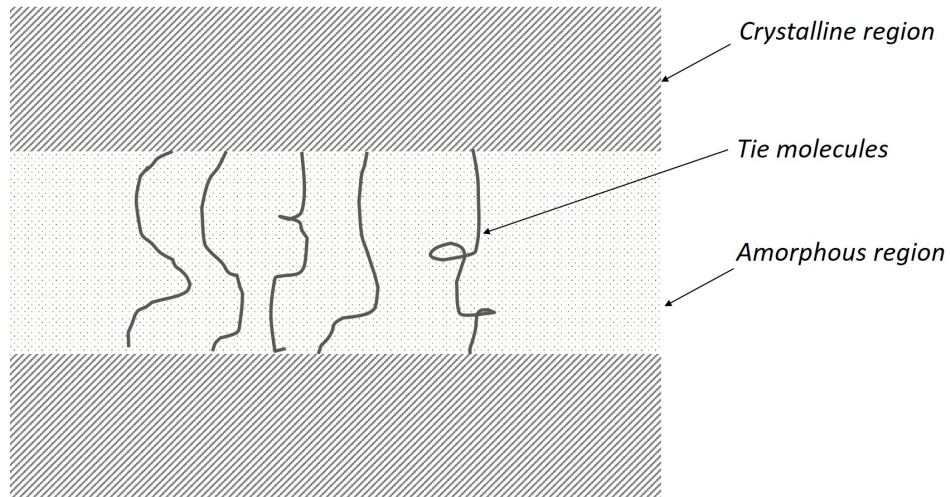


Figure 4.4: Model of a semicrystalline polymer

For a semicrystalline polymer like PE, both the crystalline and amorphous state may contribute to the material strength (See Fig 4.4). At room temperature, which is well above

the material glass transition temperature T_g , the amorphous region is liquid-like and the Van der Waals bonding is close to zero. Therefore, the load carrying capacity is primarily attributed to the crystalline regions, which are joined together via tie-molecules. Huang et al. [30] proposed that at room temperature, the strength of semicrystalline polyethylene is proportional to the number of tie-molecules, which is a linear function of weight average molecular weight M_w . In addition, a threshold molecular weight M_c was identified, below which no tie molecules can form. Hence, based on the molecular structure of polyethylene, the material strength can be considered proportional to M_w . In the context of CZM, τ_{max} is representative of the strength. Therefore, the following relation is proposed:

$$\tau_{max} \propto (M_w - M_c) \quad (4.23)$$

In the classical theory of damage mechanics, a scalar parameter ω is often used to denote the extent of damage. When the material is at its undegraded state, ω equals zero. As damage progresses, ω increases and reaches unity as the material is completely degraded. In this study, we adopt the similar concept, and define the damage parameter ω as a function of molecular weight:

$$\omega = 1 - \langle M_w - M_c \rangle / (M_w^0 - M_c) \quad (4.24)$$

where $\langle x \rangle = \max(x, 0)$, M_w is the molecular weight of the degraded state, and M_w^0 represents the undegraded state. The peak traction τ_{max} is defined as a function of ω ¹:

$$\tau_{max} = \tau_{max}^0 (1 - \omega) \quad (4.25)$$

Similarly, τ_{max}^0 is the strength of the undegraded material. The loss of molecular weight also results in a rapid reduction of toughness. A previous study by Choi et al. suggests that a power law relation exists between the toughness and damage parameter [6]:

$$G_{Ic} = G_{Ic}^0 (1 - \omega)^m \quad (4.26)$$

¹This definition of τ_{max} is intended for modeling purposes. Physically, the material strength may not drop to zero when it becomes degraded.

where G_{Ic}^0 is the toughness of undegraded material. For PE, the constant m was found to be 2.4, and is adopted in this study.

The reduction in material toughness with decreasing molecular weight reflects the transition of the overall mechanical behavior from ductile to brittle. A characteristic length l_{ch} has been commonly used to describe the extent of ductility. It is defined as a function of elastic modulus, fracture energy, and strength.

$$l_{ch} = \frac{EG_{Ic}}{\tau_{max}^2} \quad (4.27)$$

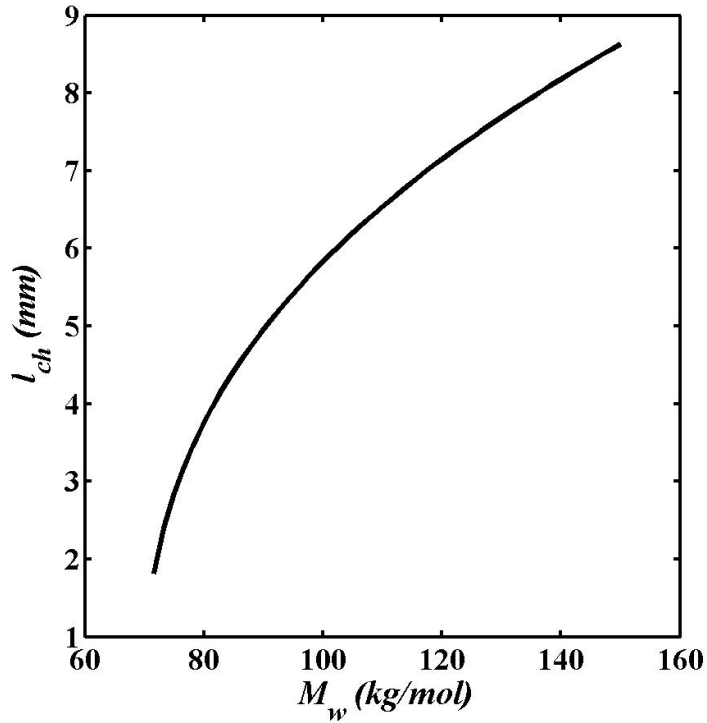


Figure 4.5: The characteristic length as a function of molecular weight

Eqn 4.27 indicates that l_{ch} is linearly proportional to the fracture energy, and inversely proportional to the squared strength. E refers to the elastic modulus in the CZM. A large characteristic length indicates high ductility. Assuming E remains a constant regardless of change in M_w , l_{ch} can be calculated as a function of M_w . This relationship is illustrated in Fig 4.5. It can be seen that the l_{ch} drops dramatically with decreasing M_w . Therefore, the

proposed molecular weight dependence of CZM is able to capture the change of ductility during the degradation of PE.

Chapter 5

Determination of model parameters

In the framework of the chemo-mechanical model, parameters for each sub-model must be determined. In the present study, tensile testing of HDPE dogbone specimens has been performed at various strain rates to find the viscoplastic model constants. The CZM parameters of the undegraded HDPE are calibrated with the fracture tests done by Kwon et al. [35]. The chemical kinetics and diffusion coefficients are calculated based on the constants provided by Colin et al.[11].

5.1 Viscoplastic constitutive model

To obtain the parameters of the viscoplastic constitutive model, uniaxial tensile testing of micro-tensile HDPE specimens have been performed. In each test, a constant strain rate is maintained on the specimen. The specimens have been tested under various strain rates ($1.36 \times 10^{-2}/s$, $1.36 \times 10^{-3}/s$, $1.36 \times 10^{-4}/s$), so that an accurate extrapolation of the viscoplastic behavior can be achieved. From the experimental test data, true stress and true strain relationships have been calculated with the aid of digital image analysis. Thereafter, the set of true stress and strain data are fitted to the viscoplastic model using

a Matlab program. In addition, the viscoplastic model is used to predict the strain history of micro-tensile specimens under creep for validation.

5.1.1 Determination of viscoplastic model parameters

In this study, 1/16" thick HDPE sheets were acquired from McMaster-Carr, an online industrial products supplier. Micro-tensile test specimens were prepared from the sheets by die-cutting. The specimen has a width of 5mm and a length of 40mm, conforming to the standard ASTM D-1708 (a standard method for the tensile properties of plastics). All the specimens have been painted white for better contrast in video capturing. Both the sample preparation and testing have been performed under room temperature (20°C).

The engineering stress (σ_e) and strain (ϵ_e) directly obtained from machine testing can commonly be converted to true stress (σ_t) and true strain (ϵ_t) with the relations:

$$\epsilon_t = \ln(1 + \epsilon_e) \quad (5.1)$$

$$\sigma_t = \sigma_e(1 + \epsilon_e) \quad (5.2)$$

However, caution should be used when implementing these relations. The underlying assumption of this conversion is that:

1. The specimen has a constant width within the gauge length
2. The specimen undergoes uniform deformation during testing

The micro-tensile testing specimen has a dogbone-shape (this will be referred to as the dogbone specimen later on), which is narrower in the center. The challenge to apply the conversion is that HDPE undergoes significant necking during tensile testing. Therefore, the true stress and true strain of HDPE cannot be directly calculated from engineering stress and strain.

An alternative approach is to utilize video imaging during testing. This technique enables

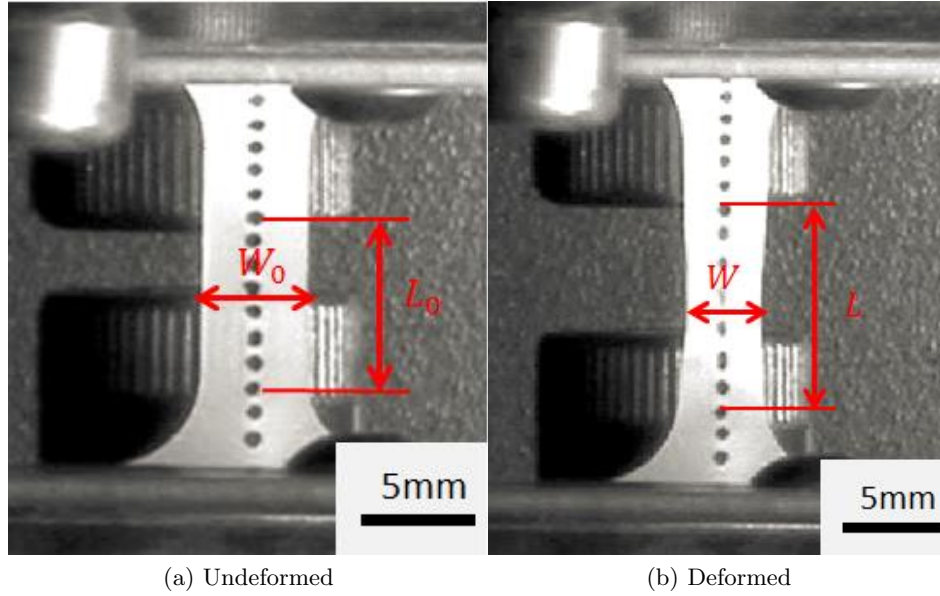


Figure 5.1: Deformation of a dogbone specimen during tensile testing

accurate evaluation of the in-plane specimen deformation at any instant. The true stress can only be calculated with the smallest cross sectional area. The smallest specimen width that occurs in the necked region can be directly measured from the image. In addition, the true strain can also be obtained by tracking the relative displacement of particular positions in the necked region. Fig 5.1 shows the dogbone specimen in both the undeformed and deformed states. As can be seen, black dots are painted along the longitudinal direction to facilitate tracking of specimen elongation. The original width and gauge length are denoted by W_0 and L_0 . After deformation initiates, the width and gauge length are W and L respectively. As the sample elongates (Fig 5.1b), necking occurs and causes the width to contract locally. This transition to necking depends on the strain rate: higher strain rate leads to earlier initiation of necking. The extent of contraction in sample width is also evaluated from video. The percentage of contraction in the thickness direction is assumed to be identical to that in the width. Therefore, the width and thickness are related:

$$\frac{W}{W_0} = \frac{T}{T_0} \quad (5.3)$$

where T_0 and T are the specimen thickness before and after deformation. The contraction

in the thickness direction can be readily inferred from the contraction in the width. The true stress σ_t and true strain ϵ_t are calculated:

$$\sigma_t = \frac{F}{W \cdot T} = \frac{F}{W \cdot T_0 \cdot (W/W_0)} \quad (5.4)$$

$$\epsilon_t = \ln\left(1 + \frac{L - L_0}{L_0}\right) \quad (5.5)$$

In the model theory section, it has already been shown that the hardening state variable X can be characterized by two equivalent formulations (Eqn 4.9 and Eqn 4.11). At each strain rate, plastic work W^p and plastic strain rate $\dot{\epsilon}^p$ are determined from true stress and strain data. The uniaxial plastic strain ϵ^p is calculated from:

$$\epsilon^p = \epsilon_t - \sigma_t/E \quad (5.6)$$

The plastic strain rate $\dot{\epsilon}^p$ can thus be determined by taking the time derivative of ϵ^p . The plastic work is:

$$W^p = \int \sigma_t d\epsilon^p \quad (5.7)$$

To determine the model parameters, a Matlab function *fminsearch* was adopted to minimize the total discrepancy of the X values calculated by both formulations for all strain rates, with initial values of the material constants taken from Zhang et al. [51]. The optimized model parameters are listed in Table 5.1.

Table 5.1: Viscoplastic constitutive model parameters at 20°C

Parameter	Value at 20°C	Parameter	Value at 20°C
E	1150MPa	d_1	9.67×10^{-4}
C	0.01	d_2	3.59
n	8	d_3	0.019
β	4×10^{-5} MPa	X_0	1MPa
γ	1×10^{-4} MPa	ν	0.38

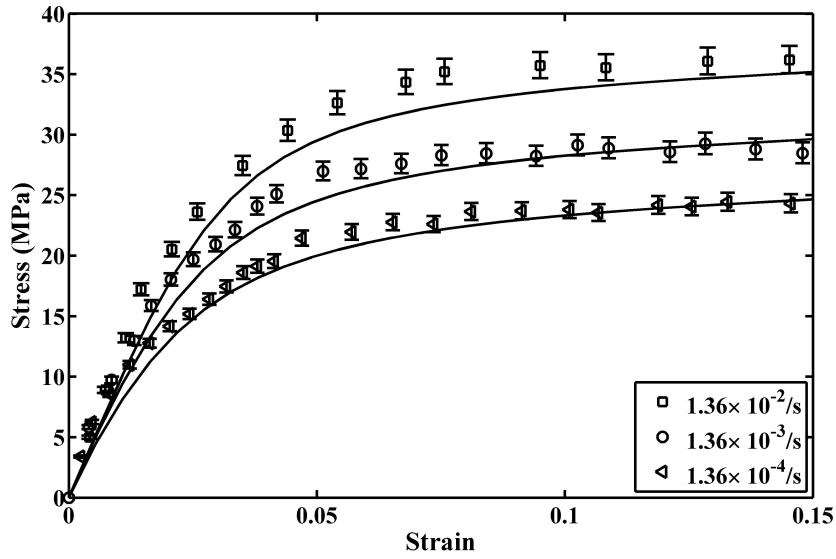


Figure 5.2: True stress and strain relations of HDPE at various strain rates

With the determined model parameters, a Matlab code was used to predict the true stress and strain relations at the testing strain rates. Fig 5.2 shows the experimental true strain and strain curves at various strain rates, as well as the predictions made by the viscoplastic model. Note that the true stress has been characterized for up to a strain limit of 15%, which was also adopted by Zhang et al. [51]. The errors are generated by the displacement evaluations from video images. There is good agreement between the experiment data and the fitting at all 3 strain rates. Hence, the viscoplastic model is able to predict the rate-dependent stress and strain relations of undegraded HDPE at various loading rates.

5.1.2 Simulation of strain history during creep loading

Creep tests were performed on HDPE specimens that had the same geometry as those used in parameter determination. All the experiments were conducted at 20°C . The testing apparatus is shown in Fig 5.3. The vertical displacement of the upper gripper was measured with a linear variable differential transformer (LVDT). The true strain was evaluated from the LVDT data. Samples were tested under stress levels ranging from 5.2 to 11.7 MPa. At a stress level above this range, necking initiated during testing, therefore the true strain evaluated from LVDT was inaccurate. The selected range of stress levels is also comparable

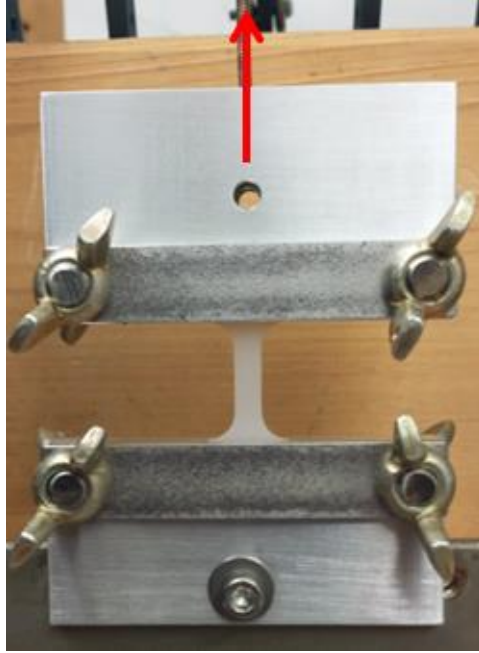


Figure 5.3: The creep testing apparatus

with other studies (Liu et al. [37], Zhang et al. [51]).

With the viscoplastic model, the strain history of specimens under various stress levels are predicted (continuous lines) and compared with experimental results (discrete symbols) as shown in Fig 5.4). The error bars correspond to a displacement of approximately 0.1mm¹. At the beginning of each creep test, strain increases rapidly due to the sudden application of a constant load. Thereafter, the total strain accumulates at a constant rate, ranging from $2.4 \times 10^{-7}/s$ at 5.2MPa to $1.2 \times 10^{-6}/s$ at 11.7MPa. Similar strain rates have been reported by other researchers. Liu et al. [37] performed creep tests on samples prepared from HDPE pipes. The corresponding creep strain rates were $3.56 \times 10^{-7}/s$ at 5.86MPa, and $1.67 \times 10^{-6}/s$ at 11.57MPa². The results indicate that the viscoplastic model can predict the creep behavior of HDPE.

¹This error is estimated from displacement tolerance when the load is applied.

²The creep strain rates are extrapolated from Figure 1 in [37]

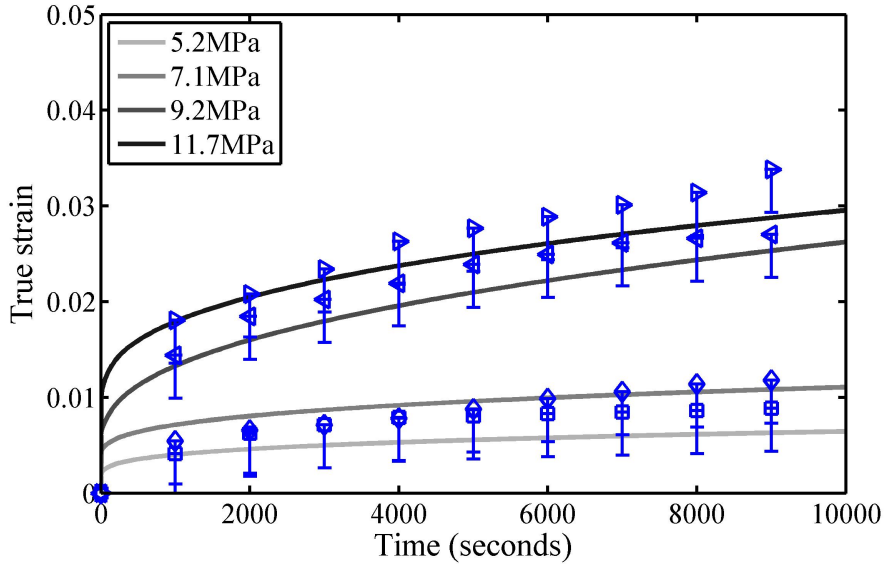


Figure 5.4: The strain history of dogbone specimens under creep

5.2 Cohesive zone model parameters for HDPE

For a cohesive zone model with a bilinear traction separation relation, only two parameters must be determined: τ_{max} and G_{Ic} . In our study, τ_{max}^0 and G_{Ic}^0 (Eqn 4.25 and 4.26) represent the undegraded properties. The parameter calibration was performed based on tensile test data of double edge notched (DEN) HDPE specimens reported in the literature [35]. The specimens were 12.5mm thick commercially extruded HDPE plates acquired from McMaster Carr. This material is identical with the material used to extract the stress-strain relations. The ligament lengths varied between 4 and 12mm.

Typically, researchers utilize *thin* DEN polymer specimens in fracture experiments to extract the fracture toughness under the plane-stress state, which is significantly greater than the plane strain toughness. The ultra high ductility of PE enables the specimen to undergo very large out-of-plane deformation when the thickness is small with respect to the ligament length. By contrast, when the thicknesses are greater than the ligament length, the specimens approach the plane strain state, and the failure mode is brittle [35]. This type of fracture is similar to SCC of polymer pipes, which occurs in plane strain conditions. For thickness to ligament length ratios greater than 1 ($T/L > 1$), the stress state approaches

the plane strain condition. For the special case of pipes, T corresponds to the total pipe length, while L is equal to the pipe wall thickness. Thus, the DEN specimens utilized in fracture parameter calibration [35], where $T/L > 1$, are acceptable for use in the simulation of crack growth in pipes.

It is clear that τ_{max} denotes the material strength prior to damage initiation. In a constant crosshead speed tensile test, the applied load increases monotonically until the peak is reached. Thereafter, the crack grows through the entire ligament, accompanied by damage propagation. The nominal section strength is defined as normalized maximum load (F_{max}) with respect to ligament area: $\sigma_{nom} = F_{max}/(T \cdot L)$. Accordingly, τ_{max} can be found at the instant of peak load. However, the magnitude of σ_{nom} varies with ligament length. Based on the tensile testing data of DEN samples in [35], σ_{nom} increases monotonically with decreasing ligament length as shown in Fig.5.5. Hence, τ_{max} for plane strain condition can be obtained by extrapolating σ_{nom} to $L \rightarrow 0$, in which case the entire ligament would have a constant stress profile. Therefore, τ_{max} is equal to σ_{nom} for $L \rightarrow 0$. In our study, $\tau_{max}^0 = 40MPa$ will be utilized for the strength of undegraded material.

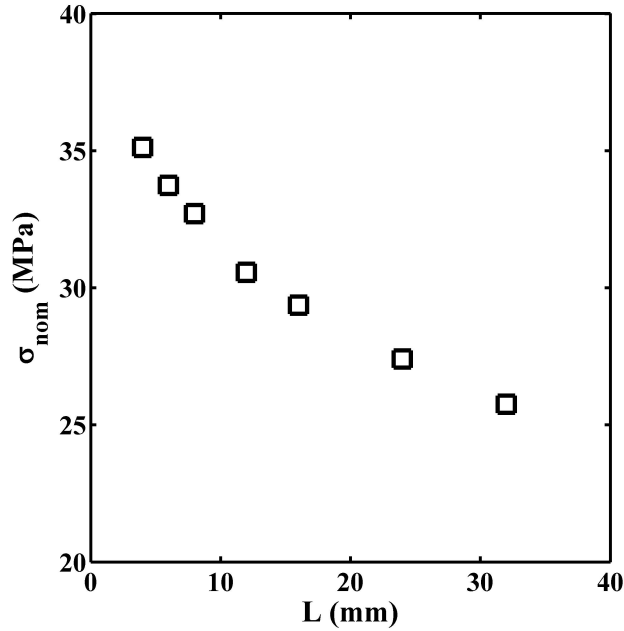


Figure 5.5: Nominal section strength as a function of L (plotted using data from [35])

After τ_{max}^0 is determined, the fracture energy is determined by matching the predicted

peak load with experiments. Using data from [35] for the 4mm ligament specimen, G_{Ic}^0 is curve fit to be $12MPa \cdot mm$. Due to the great variety of data extrapolation approaches, plane strain fracture toughness varies from below $6MPa \cdot mm$ [35], to greater than $20MPa \cdot mm$ [45]. Hence, $12MPa \cdot mm$ is a reasonable fracture toughness value for numerical simulation.

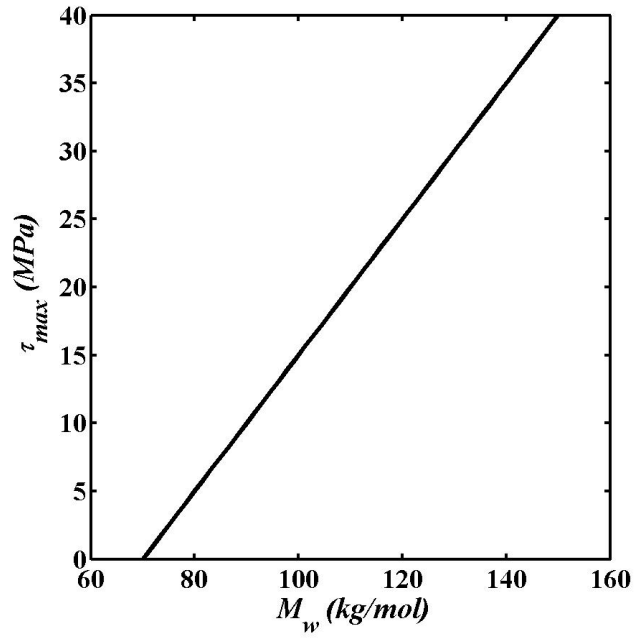
To successfully simulate the mechanical property loss due to chain scission of HDPE, the threshold value of the molecular weight M_c must be determined. Colin et al. pointed out that when the weight average molecular weight of PE drops below $70kg/mol$, cracks initiate and propagate easily, regardless of its initial molecular weight [11]. Therefore, $M_c = 70kg/mol$ is used in the numerical simulation. Given the assumption of M_c , the cohesive parameters τ_{max} and G_{Ic} are calculated as a function of M_w . The results are shown in Fig.5.6. Here, an initial molecular weight of $150 kg/mol$ is considered for the undegraded HDPE. Note that $\tau_{max}^0 = 40 MPa$ and $G_{Ic}^0 = 12 MPa \cdot mm$ are used for strength and toughness.

5.3 Chemical reaction and diffusion constants

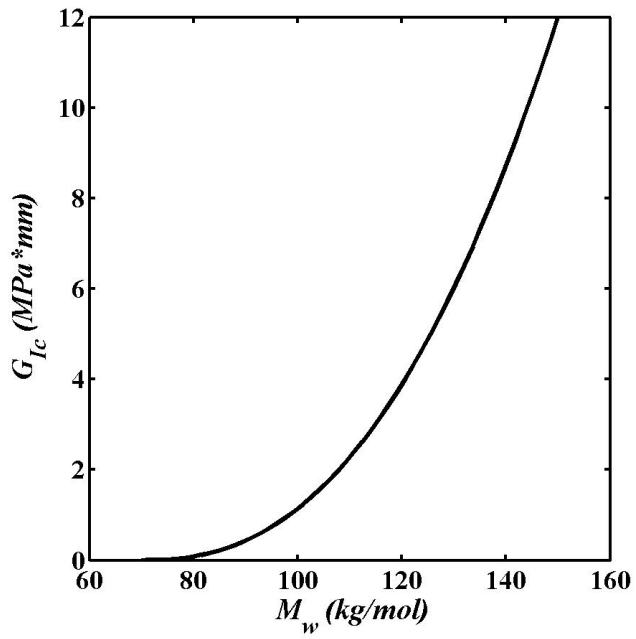
The chemical reaction and diffusion constants published in [10] and [11] are adopted in this study. The rate constants k have been reported at $40^\circ C$ in [10], and the coefficients of diffusion are listed in [11] for O_2 , DOC and AO. In this study, all simulations were performed for $20^\circ C$. Thus, these parameters were evaluated for this temperature based on Arrhenius relationship:

$$\bar{k} = Ae^{-E_a/RT} \quad (5.8)$$

where \bar{k} represents a kinetic parameter. The activation energy E_a and the prefactor A are empirical constants for parameter \bar{k} . T is the absolute temperature, and R is the universal gas constant. The rate constants are listed in Table 5.2. The coefficients of diffusion are given in Table 5.3. The yield ratios are given in Table 5.4.



(a) τ_{max} vs. M_w



(b) G_{Ic} vs. M_w

Figure 5.6: Molecular weight dependence of τ_{max} and G_{Ic}

Table 5.2: Rate constants at 20°C for kinetic modeling. Unit= $L/(mol \times s)$

Rate constant	Value at 20°C	Rate constant	Value at 20°C
k_{1u}	9.05×10^{-13}	k_{6a}	2.72×10^5
k_{1b}	5.46×10^{-10}	k_{6b}	2×10^6
k_{1d}	2.7×10^{-5}	k_{6c}	1.54×10^5
k_2	10^8	k_{6d}	3.81×10^6
k_3	1.47×10^{-3}	k_7	1.15×10^6
k_4	8×10^{11}	k_{1s}	5×10^{-2}
k_5	1.33×10^{11}	k_{s1}	1.67

Table 5.3: Coefficients of diffusion at 20°C for kinetic modeling. Unit= m^2/s

Coefficient of diffusion	Value at 20°C
D_{O_2}	2.49×10^{-11}
D_{DOC}	2×10^{-11}
D_{AH}	2.2×10^{-16}

Table 5.4: Yield ratios at 20°C

Yield ratio	Value at 20°C
γ_{1s}	1.0
γ_{1CO}	0.7
γ_4	0.5
γ_5	0.0108

Chapter 6

Numerical implementation and case study

In this chapter, FEA simulation of two types of sample geometries and loading conditions will be discussed. The objective of these simulations is two-fold:

- Demonstrate that the proposed modeling approach is applicable for various loading conditions, including monotonic load and constant stress load
- Simulate the SCC of an HDPE specimen with the chemo-mechanical modeling approach

Schematic drawings of the two cases are shown in Fig 6.1. Monotonic loading of double edge notched (DEN) specimens (see Fig 6.1a) is simulated to replicate the fracture tests done by Kwon et al. [35]. A constant displacement rate $\dot{\Delta}$ is prescribed on the upper specimen edge. To study SCC, a single edge notched (SEN) specimen (Fig 6.1b) is utilized to represent an HDPE component with an initial crack. In this case, a constant load σ is applied on the upper edge. For both SEN and DEN specimens, the bottom is fixed in all degrees of freedom, representing a clamped condition. The bold lines indicate pre-cracks, and the dashed lines represent the ligaments. Here, mode I fracture takes place and the crack will grow along the ligament, and the material property in the crack region primarily

determines the specimen fracture behavior.

6.1 Finite element analysis implementation

In the simulation of fracture for both the DEN and the SEN specimen, the FE model can be divided into two regions and modelled separately: the ligament and its surrounding regions (bulk region). CZM is implemented along the ligament with the use of 3D cohesive element type COH3D8 in Abaqus. Typically, the CZM is a phenomenological law to describe the nonlinear traction separation relationship in a specimen's *damage zone*. In finite element analysis, this is achieved by lumping the nonlinear relationship into a single layer of cohesive elements. Both a damage initiation and damage evolution criteria are assigned to a cohesive element. When the stress in the element reaches τ_{max} , damage initiation takes place. During the damage evolution phase, the interfacial displacement δ increases monotonically and the cohesive element fails when $\delta = \delta_c$. Additionally, the chemical kinetics simulation is implemented in the CZM: the reactions and diffusion are supposed to take place in a 1D space, that is, from the crack tip toward the specimen outer edge. On the other hand, the bulk region is considered not affected by chemical corrosion. Therefore, the entire corrosion-related fracture phenomenon is accounted for by the use of cohesive elements on the crack propagation path.

The bulk region is modelled with 3D hexahedral elements with reduced integration C3D8R, and the elastic-viscoplastic constitutive model (see Chapter 4.1) is utilized to predict the creep behavior of polyethylene. The constitutive model is implemented through a user defined material (UMAT) subroutine. In a UMAT program, the total incremental strain $\Delta\epsilon$ is provided. The incremental plastic strain component $\Delta\epsilon^p$ is calculated based on the flow rule. Subsequently, the incremental elastic strain component $\Delta\epsilon^e$ is obtained, and the incremental stress $\Delta\sigma$ is computed based on the tangential stiffness matrix (also known as the Jacobian). A specific algorithm of the viscoplastic model is listed in Appendix A.

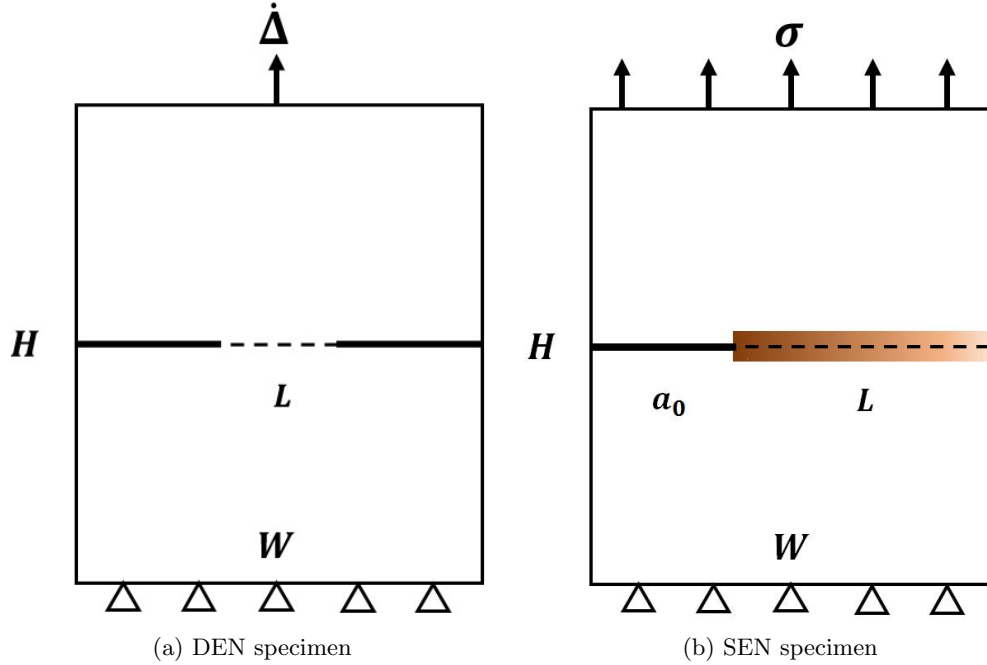


Figure 6.1: DEN and SEN specimens in finite element analysis

6.2 Simulation of monotonic loading

Kwon et al. [35] performed tensile fracture tests on double edge notched specimens using monotonic loading. The specimens were commercially extruded HDPE plates acquired from McMaster-Carr, which is the same material that we used to determine the viscoplastic model parameters. Dimensions of the specimens are 90mm (W) by 260mm (H), with a thickness (T) of 12.5mm. The FE model is created for only half of the specimen due to its geometric symmetry. The cohesive elements have a constant length of 0.5mm. To improve the computational efficiency, biased seeding was applied on the 3D hexahedral elements, with a higher density at the center of the specimen. Seed size varies between 1 and 3mm parallel to the ligament direction; while in the direction of loading, it varies between 1 and 5mm. In addition, one or multiple elements are assigned through the thickness ¹.

Two batches of specimens were prepared, with the length along both the rolling and transverse directions. In this study, tests for the transverse specimens are used as the

¹A mesh sensitivity analysis will be discussed later in Chapter 7.1.

benchmark for simulation. During the fracture testing, a constant crosshead displacement rate $\dot{\Delta} = 5\text{mm}/\text{min}$ on the upper specimen surface, and the load history is acquired through simulation.

Ligament length L of the DEN specimens varied between 2mm and 32mm. Video images were taken of the specimens during testing to show the fracture surfaces by Kwon et al. It was observed that for specimens that had a thickness to ligament length ratio (T/L) less than 1, the fracture mode was primarily brittle. This was attributed to the plane strain condition of the specimens. In this study, the fracture testing of the specimens is simulated for $L=4, 6, 8$ and 12mm.

6.3 Simulation of stress corrosion cracking

A simulation of HDPE under chlorine induced SCC is desired. The polymer component, after being exposed to a chlorinated environment, undergoes continuous chemical corrosion assisted by the diffusion of oxygen & chlorine dioxide into the sample, and antioxidant out of the sample. As the surface material becomes severely damaged, fracture takes place under stress, and the crack front inches forward. Simultaneously, the region around the crack tip that is subject to chemical reactions and diffusion also shifts its boundary toward the component core. Therefore, the following mechanisms must be simulated in a coupled fashion:

- Creep damage under a constant stress
- Reactions of oxidizers (chlorine dioxide and oxygen) with antioxidant and polyethylene
- Diffusion of oxidizers and antioxidant

As shown in Fig.6.1b, the single edge notched specimen represents the HDPE component under SCC. The left edge of the specimen is in contact with the corrosive environment, and will be referred to as the inner surface. The right edge is in contact with air, and represents the outer surface. The pre-crack represents a defect on the inner surface. The region that is affected by chemical diffusion and reactions is superimposed on the ligament (the band

with color gradient). The extent of degradation forms a gradient: the crack tip is most severely degraded (indicated by dark color), while the ligament close to the outer surface is least affected.

While the area near the crack surfaces is affected by diffusion, the structural performance is dictated by the degradation along the ligament under mode I fracture. As the crack grows along the ligament, the degraded region will expand toward the outer surface. To capture the influence of degradation, chemical kinetics simulation are performed along the *entire ligament*, and the boundary condition is updated continuously with crack propagation.

A comprehensive co-simulation approach incorporating both finite element analysis (in Abaqus 6.13) and chemical kinetics/diffusion simulation (in Matlab 2010) was developed. The procedure to implement the coupled mechanical-chemical simulation is described as follows (specific steps are summarized with a flowchart in Fig 6.2). Start the chemical kinetics and diffusion simulation by prescribing the initial condition (IC) and boundary condition (BC). This involves the assignment of the concentration of various reactants through the entire ligament. The kinetics simulation is performed in Matlab, to obtain the molecular weight profile along the crack growth path as a function of both location and time: $M_w(x,t)$. Next, the M_w profile is mapped to all the cohesive elements in Abaqus via a user defined subroutine UFIELD. This is achieved by explicitly prescribing M_w at each node of the cohesive elements as a function of time. Subsequently, finite element analysis is performed, with τ_{max} and G_{Ic} calculated for each cohesive element in every time increment based on the M_w assignment. The status of the cohesive element at the crack tip is monitored continuously, and the finite element simulation is paused when failure is detected in the cohesive element. This indicates that the crack will advance by the length of one cohesive element (0.1mm in this study).

When the crack progresses during the simulation, the IC and BC are updated accordingly in the kinetics simulation. Then, the kinetic simulation is repeated with the changed IC and BC. In general, the crack growth is simulated through this iterative process until a global failure criterion is satisfied, indicating ultimate damage of the specimen. In this study, the

failure criterion can be either one of the two scenarios, whichever occurs first:

1. the maximum principal strain in the bulk region reaches 15%,
2. unstable crack growth takes place.

With the proposed failure criteria, a conservative lifetime due to SCC can be estimated.

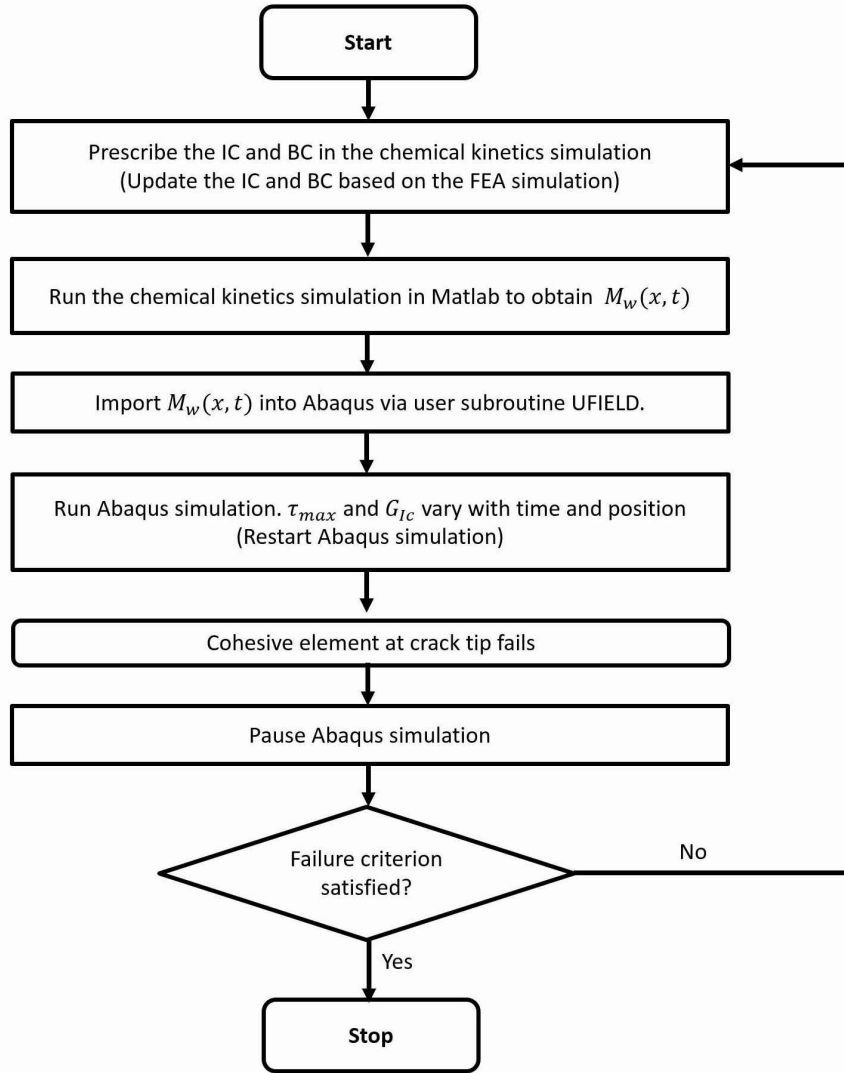


Figure 6.2: Algorithm for implementing coupled simulation of mechanical and chemical kinetics models

Dimensions of the SEN specimen used for SCC simulation are $7.3mm \times 4.5mm$ ($H \times W$), with an initial crack length $a_0 = 0.3mm$. The specimen bottom is fixed in all degrees of freedom, and a constant traction σ (varying from 0.4MPa to 7MPa) is applied on the upper

surface. In the FE model, all cohesive elements have a length of 0.1mm. All hexahedral elements have a constant seed size of 0.15mm (in the plane of deformation). The simulation of crack propagation under stress corrosion is performed for room temperature, 20°C. Three levels of chlorine dioxide concentration were investigated: 0.0005ppm, 0.01ppm, and 0.15ppm, representing increasing rates of degradation. In this study, chemical corrosion is considered to occur only at the edge that is in contact with the chlorinated solution (referred to as the inner edge). The initial concentration of oxygen in the PE is $3.8 \times 10^{-4} \text{mol/L}$, and the initial antioxidant concentration in the PE is $1.8 \times 10^{-3} \text{mol/L}$. The initial concentration of POOH and PE are 0.01mol/L and 60mol/L respectively ². All these reactants are uniformly distributed within the specimen at the initiation of chemical reactions. The initial concentration of other reactants is zero.

The boundary conditions of the chemical kinetics simulation are prescribed as follows. It is considered that an infinite amount of oxygen and DOC exist to maintain their concentrations constant at the crack tip. Therefore, the concentration of these two reactants are set to be fixed values at the crack tip. Additionally, the loss of antioxidant due to water extraction or evaporation is neglected. The flux of antioxidant at the crack tip and outer edge ($x = 4.5$) are zero (*i.e.*, $\frac{\partial[AO]}{\partial x} = 0$). The diffusion of all other reactants toward outside of the specimen is considered negligible, and the corresponding boundary conditions are prescribed similar to the antioxidant.

For each level of DOC concentration, the simulation was conducted for various stress levels. The crack growth history (*i.e.*, $a = a(t)$) and the ultimate lifetime of the specimen were obtained in each scenario. The crack growth rate da/dt was calculated using the finite difference method. The stress intensity factor K was also evaluated as a function of crack length.

²These initiation conditions were adopted from Colin et al. [11]

Chapter 7

Results and discussion

In this chapter, the results from two sets of simulation are presented and discussed. First, the fracture testing of undegraded DEN specimens is predicted and compared with the experimental data. Next, the failure mechanisms of HDPE under SCC are explored and discussed.

7.1 Monotonic load on undegraded DEN specimens

With the determined cohesive zone model parameters, fracture tests on DEN specimens provided by Kwon et al. [35] were simulated. Fig.7.1 shows the load displacement curves for 4 specimens (with various initial ligament lengths) from the published experimental data and the simulation results. The peak load in each tensile test has been accurately predicted. Note that for each experiment, the applied load dissipates dramatically after peak (stage 1), followed by a more gradual softening (stage 2). The mechanisms of the two stages in load softening were revealed by Kwon et al. [35]. In stage 1, rapid load drop occurs due to brittle fracture at the center of specimen thickness. At the same time, fibrils on the specimen surface are still connected, and undergo large plastic deformation with increasing displacement. This corresponds to the gradual post-peak load drop (stage 2). In fact, the extent of surface necking is reduced with larger T/L due to the dominance of the plane

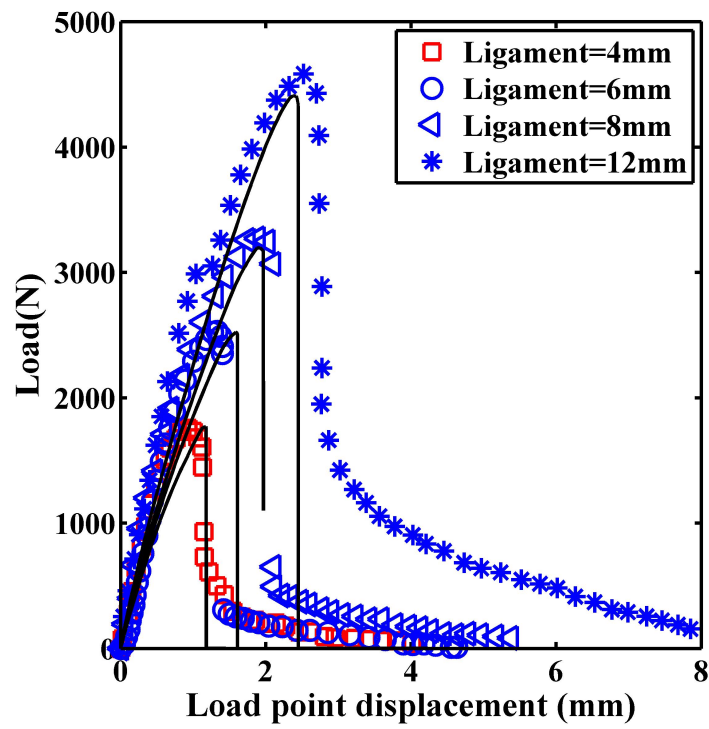


Figure 7.1: Load displacement curves for specimens of various ligament lengths. Ligament=4mm is used to calibrate G_{Ic}^0

strain condition. Hence, it can be expected that for perfect plane strain conditions, failure caused by plastic flow will be negligible compared with brittle fracture.

Only stage 1 of the load-displacement curve was predicted with our choice of CZM. Stage 2 can be accurately captured if a more sophisticated CZM softening law (such as bilinear softening) were selected. However, the failure mode in this stage is not important in the simulation of brittle fracture under SCC. Therefore, the current modeling scheme, which relies on parameters found from plane strain data, is appropriate for predicting crack growth in polymeric pipes.

Mesh size sensitivity study

In the simulation of crack propagation with cohesive elements, the length scale of elements may affect the crack growth history. Specifically, the relative size of cohesive elements with respect to 3D hexahedral elements (in the bulk region) is critical. To address this issue, a mesh size sensitivity study was performed to investigate the influence of cohesive element size.

The lengths of hexahedral elements and cohesive elements were 1mm and 0.5mm respectively in the monotonic load simulations. To study the effect of mesh density, the size of cohesive elements was reduced to 0.1mm and 0.02mm. These lengths correspond to 1/10 and 1/50 of the size of a hexahedral element. The mesh size sensitivity study was conducted on the 8mm ligament specimen. Fig 7.2 shows the simulated load-displacement curves: models with different mesh densities produce almost identical load history.

So far, only one element has been applied in the thickness direction for the monotonic loading simulations. To investigate the mesh sensitivity through the thickness, a refined meshing has been generated that includes 5 hexahedral elements through the thickness in the bulk region, and 25 cohesive elements through the thickness in the crack region. The simulated load displacement curves are shown in Fig 7.3. The result indicates that the number of elements through the thickness has a minimal influence on the load curves. Thus, the influence of mesh density on crack propagation is negligible in this study.

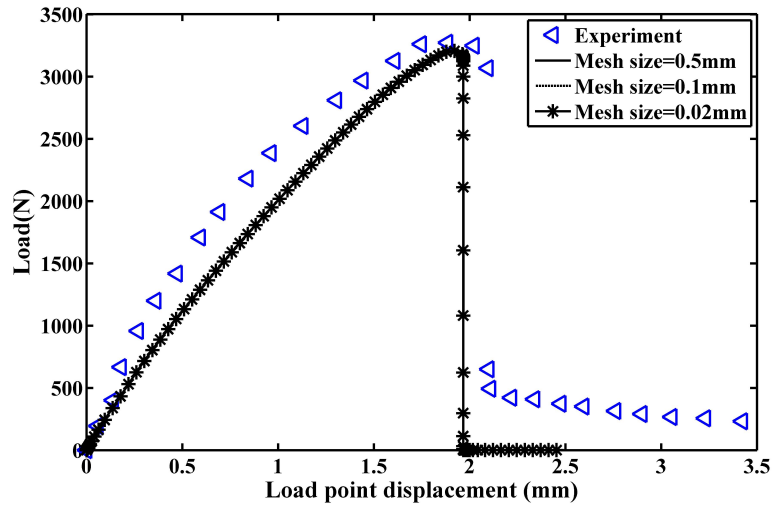


Figure 7.2: Simulated load displacement curves with various sizes of cohesive element

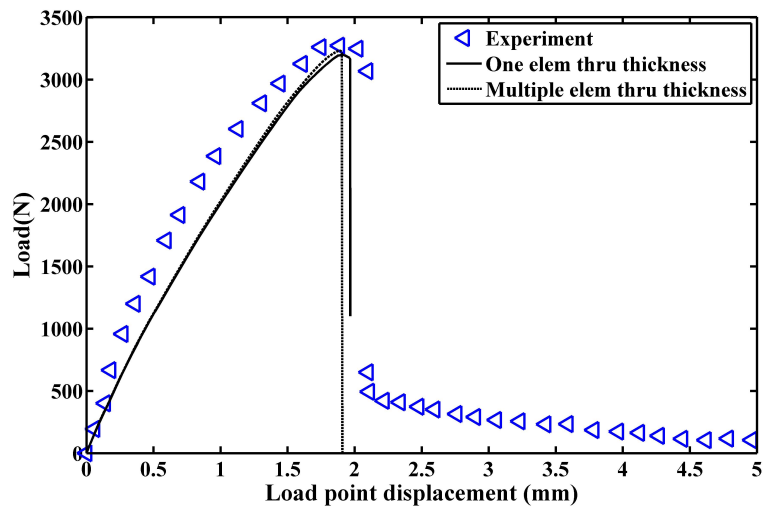
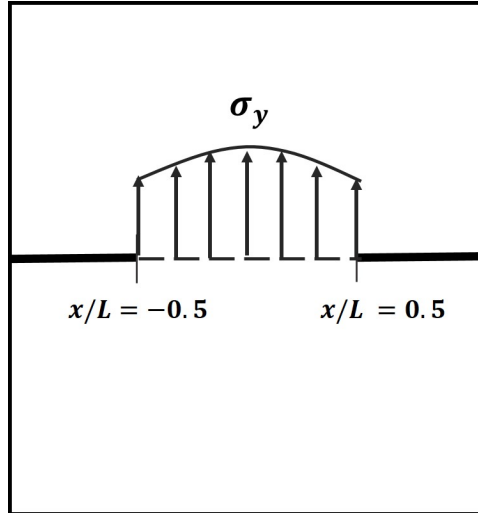
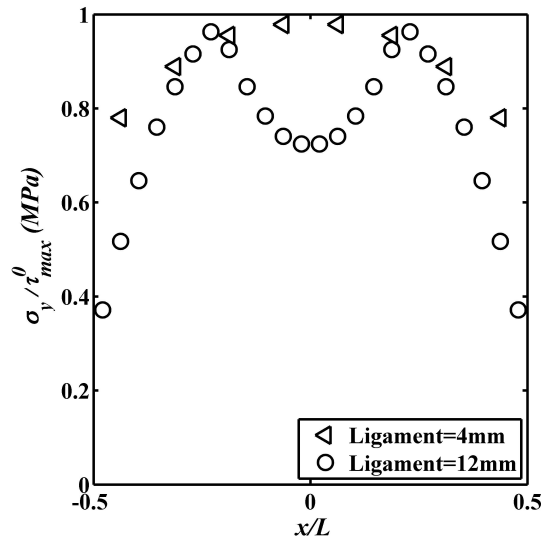


Figure 7.3: Simulated load displacement curves with various mesh densities through the specimen thickness



(a) Stress profile in the ligament of a DEN specimen



(b) Stress profile in the ligament at peak load for two specimens with ligament length = 4mm and 12mm

Figure 7.4

Stress profile along ligament

In Section 5.2, it was stated that τ_{max} can be determined by extrapolating the ligament length $L \rightarrow 0$ for a DEN specimen. The underlying reason is that as L approaches zero, the stress profile in the ligament becomes uniform. To demonstrate this point, the stress profile in an DEN specimen under monotonic loading was analyzed.

Fig 7.4a illustrates the stress profile on the entire ligament of an DEN specimen during fracture testing. σ_y denotes the stress in the direction of applied load. x represents the location along the ligament, and x/L is the normalized location. The position $x = 0$ indicates the plane of symmetry. $x/L = \pm 0.5$ is the location of crack tips. The stress profiles for two specimens, ligament=12mm and 4mm, are shown in Fig 7.4b. Here, σ_y is normalized with the material strength τ_{max}^0 . For ligament=12mm, the normalized stress level is considerably non-uniform, with σ_y less than 40% of the material strength at $x/L = \pm 0.5$. In contrast, for L=4mm, the stress profile is much more uniform through the entire ligament. This indicates that the stress variation along the ligament decreases with reduced ligament length. Therefore, it can be expected that $\sigma_y \rightarrow \tau_{max}^0$ as the ligament length approaches zero.

7.2 Constant load on SEN specimens in a chlorinated environment

In addition to simulation of the DEN specimen, crack growth in SEN specimens exposed to a chlorinated environment is also simulated. The crack length history can be extracted from each SCC simulation. Fig. 7.5 presents the crack length history for three [DOC] concentration levels, all at a stress level of 1.11MPa. Note that this level of stress is typical in a municipal water transportation system [11]. In general, the crack initiates earlier at higher [DOC] concentration due to faster chemical degradation and subsequently loss of toughness occurs. Two distinct patterns of crack propagation are shown. For [DOC]=0.15ppm and 0.01ppm, the crack growth rate is almost constant until the strain failure criterion ($\epsilon_{max} = 0.15$) is reached. In contrast, for [DOC]=0.0005ppm, the crack grows at a constant rate up to $a = 2mm$, as indicated by point A in Fig.7.5. Thereafter, the fracture accelerates until ultimate failure. In the following discussion, [DOC]=0.15ppm and 0.01ppm will be referred to as the **high concentration**, and [DOC]=0.0005ppm is the **low concentration**. The simulated results can be explained by the complex interaction between chemical reactions, diffusion, and material creep. Due to the differences in disinfectant concentration, chemical

reaction or diffusion plays a more dominant role, affecting the behavior in crack growth history. The crack growth history and polymer degradation data illustrate the effects of disinfectant concentration.

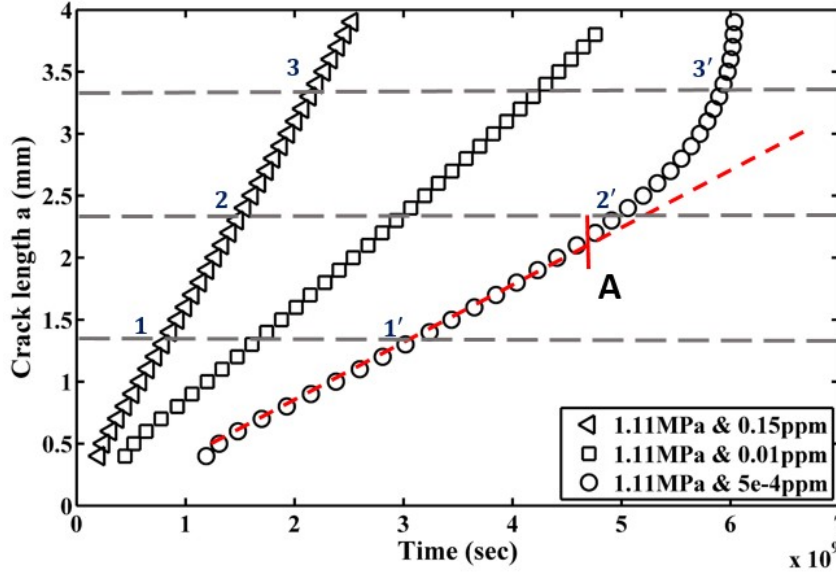
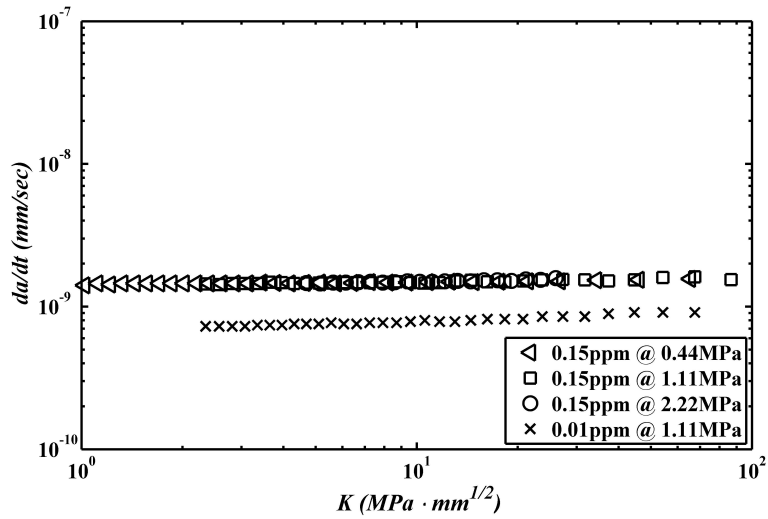


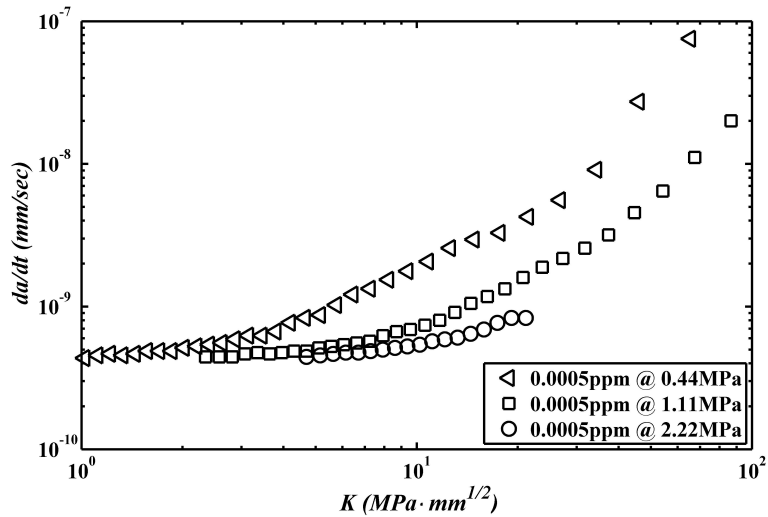
Figure 7.5: Crack growth history when stress=1.11MPa

The central difference method was used to compute the crack growth rate (da/dt) for each scenario. The results are presented as a function of stress intensity factor K around the crack tip. For the high concentration environment (Fig.7.6a), da/dt is almost a constant for both concentrations, regardless of the stress intensity factor K . This indicates that crack growth is independent of stress, and mostly induced by chemical reactions. By contrast, in the low concentration environment (Fig.7.6b), da/dt monotonically increases by almost two orders of magnitude before reaching the strain limit. In this case, crack propagation is stress driven. Another finding is that at the high concentration (eg. $[DOC]=0.15\text{ppm}$), the da/dt vs K curves at various stresses *overlap*, while at low concentration no overlapping is observed.

The evolution of the molecular weight (M_w) profile influences the crack growth behavior. Fig.7.7 presents the M_w profile through the remaining ligament when $[DOC]$ is 0.15ppm and 0.0005ppm, both at a stress level of 1.11MPa. In each scenario, the M_w profile is presented at three crack lengths (1.3mm, 2.3mm, and 3.3mm, indicated by dashed lines in



(a) High concentration set



(b) Low concentration set

Figure 7.6: Crack growth rate versus stress intensity factor for two distinct sets

Fig.7.5). Note that the crack advances to a particular length at different times. For example, $a = 1.3mm$ at either 0.8×10^9 sec for $[DOC]=0.15ppm$ (**1**), or 3.02×10^9 sec for $0.0005ppm$ (**1'**). The inner surface, where the edge of the specimen contacts the corrosive environment, is indicated by $x = 0mm$. The outer surface, which is in contact with air, is $x = 4.5mm$. It can be seen in both Fig.7.7a and Fig.7.7b, the M_w profile shifts continuously as the crack grows, and a steep molecular weight drop forms at the crack tip due to chemical reactions. However, the M_w profiles far from crack tip differ dramatically. In the high concentration environment, the M_w (and subsequently mechanical properties) is at the initial value for most of the ligament. Properties are only degraded in a narrow region approximately 0.5mm wide at the crack tip. In the low concentration environment, the M_w is severely reduced throughout the entire ligament as the crack tip advances.

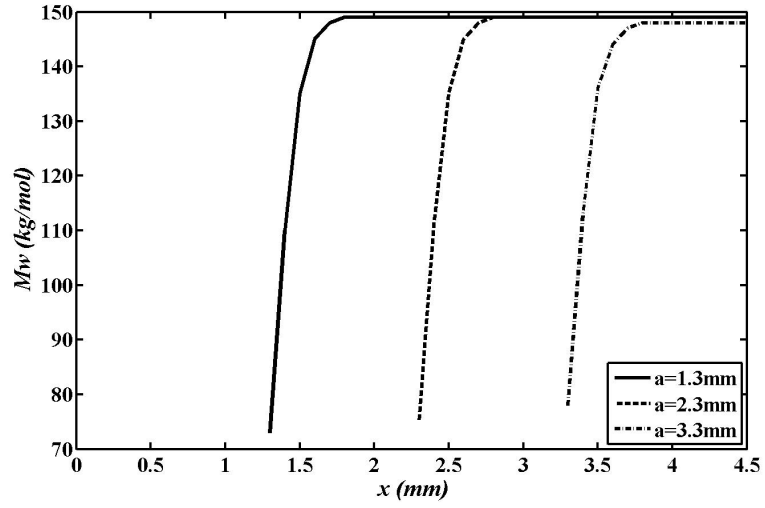
The distinction in M_w profiles at high or low disinfectant concentration is caused by the dominance of either chemical reactions or diffusion. For the high concentration scenario, chemical reactions are fast. As a result, the oxidizers are quickly depleted before they migrate far into the component, and the M_w loss is localized near the surface. On the other hand, reactions are slower at the low disinfectant concentration, and the oxidizers can diffuse farther into the remaining ligament. Therefore, as the disinfectant concentration drops, the polymer degradation mode transitions from *reaction-driven* to *diffusion-driven*.

The domination of chemical reaction or diffusion can also be confirmed from the characteristic time of each process. The characteristic time of diffusion, τ_{ch}^D , is a function of length l and diffusion coefficient D :

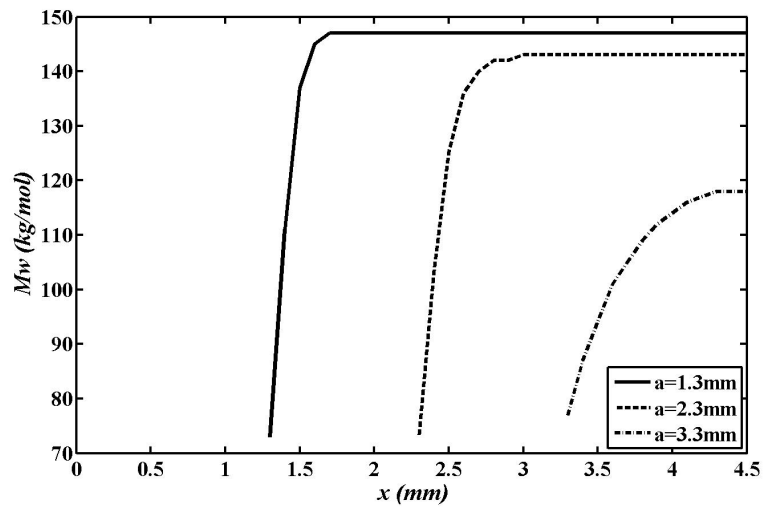
$$\tau_{ch}^D = \frac{l^2}{D} \quad (7.1)$$

The characteristic time of the chemical reaction process is defined as follows. In this study, the general extent of degradation is only measured by the reduction in polymer molecular weight. Therefore, the characteristic time of reaction ¹, τ_{ch}^R , is defined by the time it takes M_w to drop to 36.8% ($1/e$) of its initial value with respect to the threshold molecular weight M_c . Equivalently, it is the time that the damage parameter ω reaches $(e - 1)/e = 63.2\%$.

¹In fact, this characteristic time of reaction accounts for the effects of both reaction and diffusion.



(a) 0.15ppm



(b) 0.0005ppm

Figure 7.7: Molecular weight profile for (a) 0.15ppm and (b) 0.0005ppm, at three crack lengths respectively

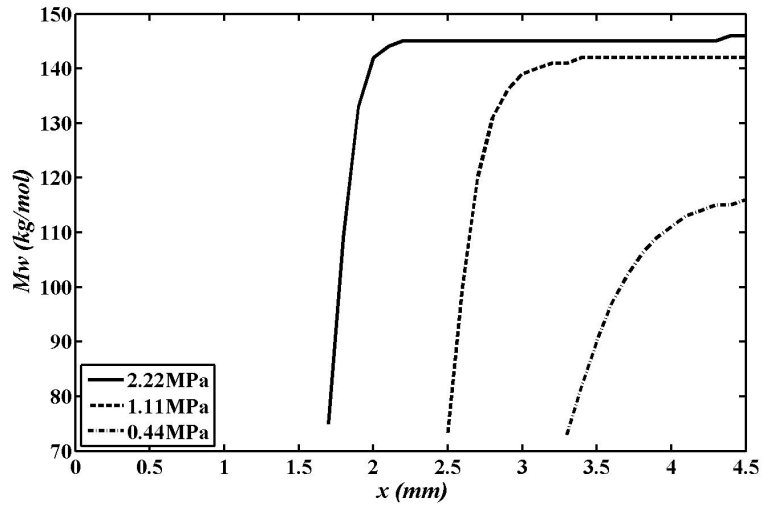
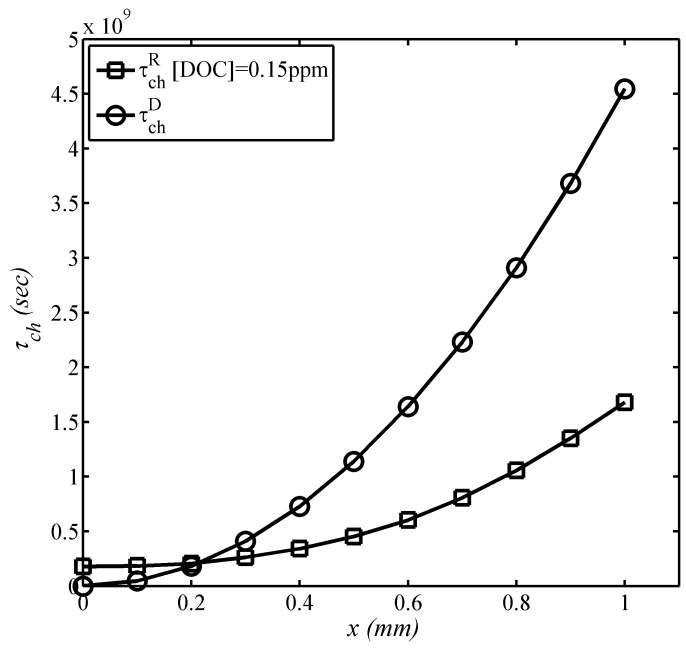


Figure 7.8: M_w profiles for $[\text{DOC}]=0.0005\text{ppm}$ at $K=10\text{MPa} \cdot \sqrt{\text{mm}}$

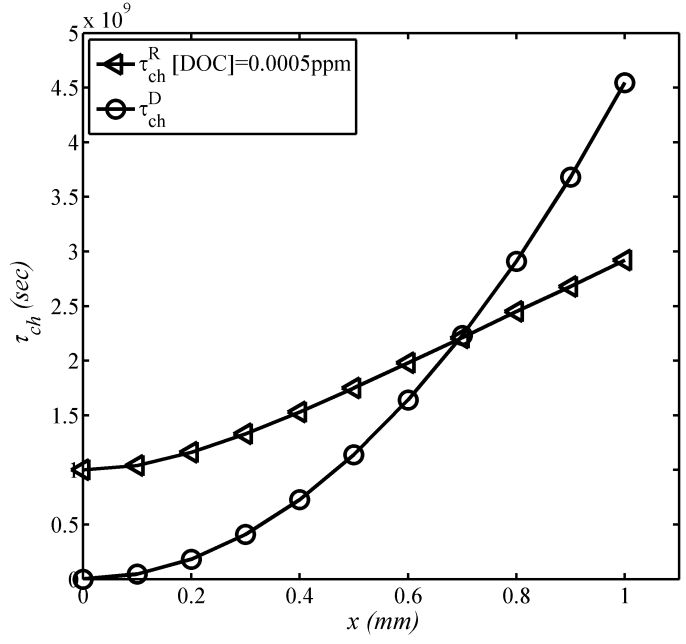
Let's consider τ_{ch}^R and τ_{ch}^D for various depths beneath the material surface for up to 1mm, in the absence of crack formation, and for two DOC concentrations: 0.15ppm and 0.0005ppm (see Fig 7.9). In this study, the diffusion of three reactants are tracked in the kinetics simulation: O_2 , Cl_2 , and DOC. The diffusion coefficient of DOC is significantly lower than the other two species due to large molecule size. Therefore, the diffusion characteristic time is considered to be dictated by DOC. It is noteworthy that τ_{ch}^D is independent of the disinfectant concentration, and increases quadratically with the depth x (Eqn 7.1).

For $[\text{DOC}]=0.15\text{ppm}$, τ_{ch}^D is shorter than τ_{ch}^R for $x < 0.2\text{mm}$ (diffusion dominant). At a depth greater than 0.2mm, the diffusion characteristic time becomes increasingly greater than the reaction characteristic time. Therefore, the chemical corrosion is primarily determined by reaction except for the area proximate to the surface ($x < 0.2\text{mm}$), where the diffusion loss of AO outweighs reactions. In contrast, diffusion dominates a larger region (for up to 0.7mm below the surface) when $[\text{DOC}]=0.0005\text{ppm}$, and the longer reaction time at a certain depth is caused by the lower disinfectant concentration. Hence, it can be generally concluded that as the disinfectant concentration decreases, chemical corrosion is increasingly dominated by diffusion.

The differences in the crack growth rate history (See Fig.7.6) can then be explained by the two polymer degradation modes. For reaction-driven crack growth, da/dt is controlled by



(a) 0.15ppm



(b) 0.0005ppm

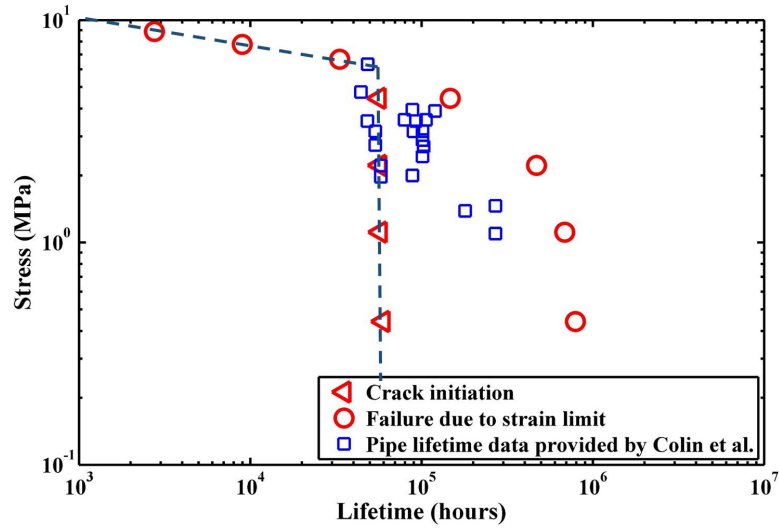
Figure 7.9: Characteristic times of diffusion and reaction for (a) 0.15ppm and (b) 0.0005ppm

the concentration of the disinfectant concentration. Therefore, da/dt is constant when the disinfectant concentration does not change (Fig.7.6a). For diffusion-driven crack growth, the monotonic increase of da/dt is predominantly influenced by the reduction of material property in the remaining ligament. In other words, crack growth is stress driven due to weakened material properties.

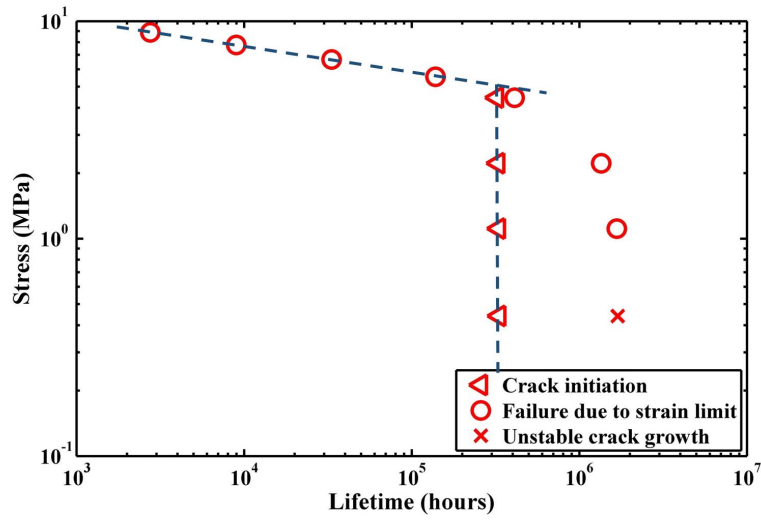
As also noted previously, the da/dt curves for the low concentration do not overlap. In fact, for a given K , crack growth rate at a lower stress level is faster. This phenomenon can also be explained by the effects of reaction and diffusion. Fig.7.8 shows the Mw profile for the three stress levels at the instant K reaches $10MPa \cdot \sqrt{mm}$ (see the dashed line in Fig.7.6b). Note that the same stress intensity factor corresponds to various crack lengths due to differences in stress level. At the lowest stress level (0.44MPa), the remaining ligament is most degraded because of long exposure time. In this case, the reduction of material property *outweighs* the influence of stress such that the crack grows fastest at this given K .

In addition to the study of crack growth history, the ultimate failure times are also investigated. For the two levels of [DOC] (0.15ppm and 0.0005ppm), simulation has been performed at various stress levels ranging from 0.44MPa to 8.9MPa. All the scenarios simulated occur at $20^{\circ}C$.

Observation of pipe failure under SCC shows the failure mode, whether ductile or brittle, depends on the level of applied stress ([11], [31], [7]). At high stresses, failure occurs in the form of localized bulging as a result of excessively large deformation. At low stresses, brittle failure takes place due to slow crack growth assisted by significant chemical degradation. In the simulation results, both of these failure mechanisms are revealed. Fig.7.10b and 7.10a present the specimen lifetimes versus stresses, both on a log scale. At high stresses, the specimen undergoes significant deformation and reaches the bulk material strain limit. This occurs when the stress is greater than 5.5MPa at [DOC]=0.0005ppm, or 6.6MPa at [DOC]=0.15ppm. On the lifetime plot, an asymptotic line is formed in this regime. This trend line has a small slope, indicating relatively significant stress dependence. At low stresses, a crack initiates (as shown by \triangleleft) and grows until failure either from large



(a) 0.15ppm



(b) 0.0005ppm

Figure 7.10: Simulated lifetime-stress relations for (a) 0.15ppm and (b) 0.0005ppm at 20°C

strain or unstable crack growth. Here, crack initiation is defined as the failure of the first cohesive element at the crack tip (zero cohesive stress). It is noteworthy that for either DOC concentration, crack initiation time is almost constant, regardless of the applied stress. This is a clear sign that crack initiation is predominantly driven by the corrosion of PE, and the effect of stress is insignificant. Additionally, crack initiation occurs at an earlier time for the high concentration as expected. These two failure modes have been categorized as *regime I* and *regime III* in the literature [11]. Regime II typically refers to the failure mode that involves slow crack growth without chemical corrosion. This type of failure was not observed in our simulation results. In general, the simulation results for SCC at high and low stresses demonstrate similar failure mechanisms that are observed in regime I and regime III.

The crack propagation phase is defined as the duration from crack initiation to the instant that a failure criterion is reached. The simulation results show that when the stress is high in regime III, the crack propagation phase is relatively short. This occurs as a result of more pronounced material creep. In addition, most simulations end by the strain limit criterion except one: 0.44MPa at 0.0005ppm. In this instance, the average fracture toughness of the ligament is less than 1% of its undegraded state when failure occurs, and the energy flux is greater than the degraded fracture energy, which causes unstable crack growth under creep loading. The simulated crack propagation phase has also been compared with published pipe lifetime data. Colin et al. [11] provided the failure times of PE water pipes from south France, which varies from 5 to 30 years under various stresses (from 1 to 6MPa approximately). All the pipes have been reported to fail due to fracture. These lifetime data are comparable with the crack propagation phase predicted for [DOC]=0.15ppm (See Fig 7.10a).

In summary, the current simulation framework is capable to predict the failure of polyethylene under two loading conditions: monotonic and creep loading. Specifically, under creep loading, SCC has been successfully simulated via a co-simulation approach involving chemical reactions and diffusion calculations. Two failure mechanisms under SCC have been predicted: regime I that is due to material creep, and regime III that is controlled by oxidation reactions and diffusion. Predicted results manifested the competition of mechanical

creep and chemical induced corrosion, both of which contribute to component failure.

Chapter 8

Conclusions and future work

In this study, a simulation framework has been constructed to investigate the time-dependent crack growth in viscoplastic polymers. Specifically, a case study was performed to predict the SCC failure of HDPE in a chlorinated environment. A novel co-simulation approach has been developed to incorporate the chemical kinetics calculations from Matlab into finite element analysis in Abaqus. Two types of loading, monotonic and creep, have been successfully simulated for HDPE. In fact, due to the generic functionality of Abaqus, this numerical framework is very flexible and readily adaptable for other materials and loading conditions.

A viscoplastic constitutive model is applied to characterize the time-dependent stress and strain relation. Model parameters have been calibrated through tensile testing in a previous study. Cohesive zone model with linear softening is utilized. τ_{max}^0 and G_{Ic}^0 are determined to be $40MPa$ and $12MPa \cdot mm$ for the undegraded HDPE. Reaction induced M_w loss, and subsequently the degradation of material strength and toughness, are captured via CZM: the traction separation relation is modified to be a function of M_w . Chemical kinetics and diffusion simulation is carried out in situ with FEA, to predict the M_w profile in the specimen as the crack tip progresses. Two failure modes are considered to determine the lifetime: failure due to large strain where a strain limit of 15% is considered as a conservative criterion, and catastrophic unstable crack growth.

Results show that the failure mode in SCC is dependent on the applied load. At high stresses, the strain limit is quickly reached prior to the initiation of crack. This type of failure corresponds to the regime I on a lifetime-stress plot. At low stresses, chemical reaction tremendously corrodes the material properties over a longer time span. Therefore, failure is mainly caused by the loss of fracture property and, consequently, crack propagation. This failure mode is characteristic of the regime III brittle failure.

Two distinct crack propagation patterns have been identified due to difference in DOC concentration: reaction-driven and diffusion-driven. At a high DOC concentration, corrosion is localized around the crack tip, and crack growth rate da/dt remains almost a constant throughout the entire failure history. By contrast, da/dt increases with the progression of crack when the DOC concentration is very low. This is caused by a collective contribution from chemical diffusion and reactions over the very long time span: material integrity in the remaining ligament is severely undermined. Thus, crack growth accelerates as a result of weakening material strength and toughness.

The relative significance of diffusion and reaction was also corroborated by an analysis of characteristic time scales. A short characteristic time suggests that the corresponding process is fast. In reaction-driven crack growth, the characteristic time of diffusion is almost a order of magnitude longer than reaction, indicating the dominance of reactions. By contrast, in reaction-diffusion driven crack propagation, the characteristic times for both processes are very close. Thus, the characteristic time is an important metric that provides insight into the relative strength of diffusion and reactions without running a finite element analysis.

By using the current simulation framework, one can sufficiently explore the interactions of disinfectant concentration, loading, and even temperature in SCC analysis. The framework is also general enough to implement with other chemical reaction and diffusion models.

In the future, the proposed chemo-mechanical modeling approach may be expanded to analyze the performance of a variety of polymeric materials under stress corrosion. For a particular polymer, the relationships between molecular weight and fracture properties

(such as τ_{max} and G_{Ic}) can be determined experimentally. To do this, thin film specimens may be prepared and exposed to a controlled oxidizing environment to obtain uniform degradation through the thickness. The exposure time can be varied to achieve a spectrum of corrosion levels. The molecular weight and polydispersity index of the degraded polymer can be measured via gel permeation chromatography. Meanwhile, tensile fracture testing may be used to determine the fracture properties. These data can be used to construct the molecular weight dependence of CZM for any polymer.

So far, the modeling approach is based on a deterministic framework. However, randomness exists in all aspects of a structural application that involves stress corrosion. For instance, the diffusivity of a disinfectant in a semi-crystalline polymer may vary significantly due to the nature of the material. In addition, the variability associated with the molecular weight also introduces variance into material properties. Furthermore, external factors such as temperature and load may undergo cyclical variations, which bring even more uncertainties into the structural analysis. Hence, a stochastic method should be included in the chemo-mechanical model to generate a reliability-based analysis and provide a probabilistic estimate of lifetime.

Bibliography

- [1] *Mechanical behavior of materials*. Cambridge University Press, 2009.
- [2] L Audouin, V Langlois, J Verdu, and J De Bruijn. Role of oxygen diffusion in polymer ageing: kinetic and mechanical aspects. *Journal of Materials science*, 29(3):569–583, 1994.
- [3] S Bodner and Y Partom. Constitutive equations for elastic-viscoplastic strain-hardening materials. *Journal of Applied Mechanics*, 42(2):385–389, 1975.
- [4] W Chan and J Williams. Determination of the fracture toughness of polymeric films by the essential work method. *Polymer*, 35(8):1666–1672, 1994.
- [5] B Choi, A Chudnovsky, and K Sehanobish. Stress corrosion cracking in plastic pipes: observation and modeling. *International Journal of Fracture*, 145(1):81–88, 2007.
- [6] B Choi, Z Zhou, A Chudnovsky, S Stivala, K Sehanobish, and C Bosnyak. Fracture initiation associated with chemical degradation: observation and modeling. *International Journal of Solids and Structures*, 42(2):681–695, 2005.
- [7] A Chudnovsky, Z Zhou, H Zhang, and K Sehanobish. Lifetime assessment of engineering thermoplastics. *International Journal of Engineering Science*, 59:108–139, 2012.
- [8] O Colak and N Dusunceli. Modeling viscoelastic and viscoplastic behavior of high density polyethylene (hdpe). *Journal of Engineering Materials and Technology*, 128(4):572–578, 2006.

- [9] X Colin, L Audouin, and J Verdu. Towards a non empirical lifetime prediction of polyethylene pipes used for the transport of drinking water. *EUROPEAN JOURNAL OF ENVIRONMENTAL AND CIVIL ENGINEERING*, 13(9):1017–1028, 2009.
- [10] X Colin, L Audouin, J Verdu, M Rozental-Evesque, B Rabaud, F Martin, and F Bourguine. Aging of polyethylene pipes transporting drinking water disinfected by chlorine dioxide. i. chemical aspects. *Polymer Engineering & Science*, 49(7):1429–1437, 2009.
- [11] X Colin, L Audouin, J Verdu, M Rozental-Evesque, B Rabaud, F Martin, and F Bourguine. Aging of polyethylene pipes transporting drinking water disinfected by chlorine dioxide. part i lifetime prediction. *Polymer Engineering & Science*, 49(8):1642–1652, 2009.
- [12] ASTM Standard D1693. Standard test method for environmental stress-cracking of ethylene plastics. *American Society of Testing and Materials*, 2008.
- [13] ASTM Standard D5397. Standard test method for evaluation of stress crack resistance of polyolefin geomembranes using notched constant tensile load test. *American Society of Testing and Materials*, 2012.
- [14] ASTM Standard D5747. Standard practice for tests to evaluate the chemical resistance of geomembranes to liquids. *American Society of Testing and Materials*, 2013.
- [15] Rhode Island USA Dassault Systemes, Providence. Abaqus documentation, 2011.
- [16] J Dear and N Mason. Effect of chlorine on polyethylene pipes in water distribution networks. *Proceedings of the Institution of Mechanical Engineers, Part L: Journal of Materials Design and Applications*, 220(3):97–111, 2006.
- [17] C Devilliers, B Fayolle, L Laiarinandrasana, S Oberti, and E Gaudichet-Maurin. Kinetics of chlorine-induced polyethylene degradation in water pipes. *Polymer degradation and stability*, 96(7):1361–1368, 2011.
- [18] A Drozdov and J Christiansen. Viscoelasticity and viscoplasticity of semicrystalline polymers: Structure–property relations for high-density polyethylene. *Computational*

- materials science*, 39(4):729–751, 2007.
- [19] D Duvall and D Edwards. Field failure mechanisms in hdpe potable water pipe. In *Society of Plastic Engineers ANTEC 2011*.
- [20] D Duvall and D Edwards. Oxidative degradation of high density polyethylene pipes from exposure to drinking water disinfectants. Technical report, Engineering Systems Inc., 2009.
- [21] JM Eagle. <http://www.jmeagle.com/plastic-pipe/pe-pipe/mdpe-yellow-gas.html> retrieved october 16, 2015.
- [22] M Elices, G Guinea, J Gomez, and J Planas. The cohesive zone model: advantages, limitations and challenges. *Engineering fracture mechanics*, 69(2):137–163, 2002.
- [23] ASTM Standard F2136. Standard test method for notched, constant ligament-stress (ncls) test to determine slow-crack-growth resistance of hdpe resins or hdpe corrugated pipe. *American Society of Testing and Materials*, 2008.
- [24] Freedonia Group. World plastic pipe to 2017 - demand and sales forecasts, market share, market size. *Market Leaders*.
- [25] H Hamouda, L Laiarinandrasana, and R Piques. Viscoplastic behaviour of a medium density polyethylene (mdpe): Constitutive equations based on double nonlinear deformation model. *International journal of plasticity*, 23(8):1307–1327, 2007.
- [26] H Hamouda, M Simoes-Betbeder, F Grillon, P Blouet, N Billon, and R Piques. Creep damage mechanisms in polyethylene gas pipes. *Polymer*, 42(12):5425–5437, 2001.
- [27] S Hashemi. Fracture toughness evaluation of ductile polymeric films. *Journal of materials science*, 32(6):1563–1573, 1997.
- [28] Y Hsuan, P Gurian, and J Zhang. Factors affecting stress crack resistance of corrugated high-density polyethylene pipe. *Transportation Research Record: Journal of the Transportation Research Board*, (2028):183–191, 2007.

- [29] Y Hsuan, R Koerner, and A Lord Jr. Stress-cracking resistance of high-density polyethylene geomembranes. *Journal of geotechnical engineering*, 119(11):1840–1855, 1993.
- [30] Y Huang and N Brown. The effect of molecular weight on slow crack growth in linear polyethylene homopolymers. *Journal of materials science*, 23(10):3648–3655, 1988.
- [31] P Hutař, M Ševčík, L Náhlík, G Pinter, A Frank, and I Mitev. A numerical methodology for lifetime estimation of hdpe pressure pipes. *Engineering fracture mechanics*, 78(17):3049–3058, 2011.
- [32] B Klemann and T DeVilbiss. The fracture toughness of thin polymeric films. *Polymer Engineering & Science*, 36(1):126–134, 1996.
- [33] R Krishnaswamy. Analysis of ductile and brittle failures from creep rupture testing of high-density polyethylene (hdpe) pipes. *Polymer*, 46(25):11664–11672, 2005.
- [34] S Kurtz, C Rimnac, T Santner, and D Bartel. Exponential model for the tensile true stress-strain behavior of as-irradiated and oxidatively degraded ultra high molecular weight polyethylene. *Journal of orthopaedic research*, 14(5):755–761, 1996.
- [35] H Kwon and P Jar. New energy partitioning approach to the measurement of plane-strain fracture toughness of high-density polyethylene based on the concept of essential work of fracture. *Engineering Fracture Mechanics*, 74(16):2471–2480, 2007.
- [36] R Lang, A Stern, and G Doerner. PREDICTION MODELS FOR THERMOPLASTICS PIPES UNDER INTERNAL PRESSURE. 247:131–145, 1997.
- [37] H Liu, M Polak, and A Penlidis. A practical approach to modeling time-dependent nonlinear creep behavior of polyethylene for structural applications. *Polymer Engineering & Science*, 48(1):159–167, 2008.
- [38] X Lu and N Brown. The ductile-brittle transition in a polyethylene copolymer. *Journal of materials science*, 25(1):29–34, 1990.

- [39] Y Mai and P Powell. Essential work of fracture and j-integral measurements for ductile polymers. *Journal of Polymer Science Part B: Polymer Physics*, 29(7):785–793, 1991.
- [40] S Maiti and P Geubelle. A cohesive model for fatigue failure of polymers. *Engineering Fracture Mechanics*, 72(5):691–708, 2005.
- [41] Marketsandmarkets. Geomembranes market by type of technology, by materials, by applications, and geography- regional trends and forecast to 2019.
- [42] V Olden, C Thaulow, R Johnsen, E Østby, and T Berstad. Influence of hydrogen from cathodic protection on the fracture susceptibility of 25% cr duplex stainless steel—constant load sent testing and fe-modelling using hydrogen influenced cohesive zone elements. *Engineering Fracture Mechanics*, 76(7):827–844, 2009.
- [43] K Park, G Paulino, and J Roesler. Determination of the kink point in the bilinear softening model for concrete. *Engineering Fracture Mechanics*, 75(13):3806–3818, 2008.
- [44] C Paton and S Hashemi. Plane-stress essential work of ductile fracture for polycarbonate. *Journal of materials science*, 27(9):2279–2290, 1992.
- [45] A Saleemi and J Nairn. The plane-strain essential work of fracture as a measure of the fracture toughness of ductile polymers. *Polymer Engineering & Science*, 30(4):211–218, 1990.
- [46] G. Singh, S Mantell, and J Davidson. In *Solar 2011, American Solar Energy Society*.
- [47] S Song, G Paulino, and W Buttlar. Simulation of crack propagation in asphalt concrete using an intrinsic cohesive zone model. *Journal of Engineering Mechanics*, 132(11):1215–1223, 2006.
- [48] S Ting, J Williams, and A Ivankovic. Characterization of the fracture behavior of polyethylene using measured cohesive curves. i: Effects of constraint and rate. *Polymer Engineering & Science*, 46(6):763–777, 2006.
- [49] C Xu, T Siegmund, and K Ramani. Rate-dependent crack growth in adhesives: I. modeling approach. *International journal of adhesion and adhesives*, 23(1):9–13, 2003.

- [50] W Yu, B Azhdar, D Andersson, T Reitberger, J Hassinen, T Hjertberg, and U Gedde. Deterioration of polyethylene pipes exposed to water containing chlorine dioxide. *Polymer degradation and stability*, 96(5):790–797, 2011.
- [51] C Zhang and I Moore. Nonlinear mechanical response of high density polyethylene. part ii: Uniaxial constitutive modeling. *Polymer Engineering & Science*, 37(2):414–420, 1997.
- [52] F Zhou, J Molinari, and T Shioya. A rate-dependent cohesive model for simulating dynamic crack propagation in brittle materials. *Engineering Fracture Mechanics*, 72(9):1383–1410, 2005.

Appendix A

Viscoplastic model implementation in Abaqus

A numerical algorithm has been developed to implement the elastic-viscoplastic constitutive model in Abaqus. The explicit method is used in numerical integration. This algorithm has been programmed into a user defined material subroutine UMAT with Fortran. A step-by-step description of the algorithm is provided in Table A.1. For a variable VAR_t , the subscript t denotes time: VAR_t refers to the variable value at the beginning of the current time increment, and VAR_{t+1} refers to the beginning of the next time increment. Note that all tensors and vectors are in bold form.

Table A.1: Algorithm for the elastic-viscoplastic constitutive model

Steps	Implementation
1	Setup the elasticity stiffness tensor \mathbf{C}
2	Save the effective plastic strain rate and stress from the previous increment: \dot{p}_t and σ_t
3	Compute the effective stress σ_e : $\sigma_{e_t} = \sqrt{\frac{3}{2}\boldsymbol{\sigma}'_t : \boldsymbol{\sigma}'_t}$ where $\boldsymbol{\sigma}'_t = \boldsymbol{\sigma}_t - \frac{1}{3}tr(\boldsymbol{\sigma}_t)\mathbf{I}$
4	Compute the effective plastic strain rate \dot{p}_{t+1} : $\alpha = d_1 \exp(d_2 \dot{p}_t^{d_3});$ $X_{t+1} = \frac{X_0}{\alpha + \sqrt{\frac{\beta}{\gamma + W_t^p}}};$ $\dot{p}_{t+1} = c \left(\frac{\sigma_{e_t}}{X_{t+1}} \right)^n$
5	Compute the effective plastic strain increment: $\Delta p = \frac{dt}{2}(\dot{p}_t + \dot{p}_{t+1})$
6	Compute plastic strain increment: $\Delta \boldsymbol{\epsilon}^p = \Delta p * \mathbf{n} = \frac{3}{2} \Delta p \frac{\boldsymbol{\sigma}'_t}{\sigma_{e_t}}$
7	Compute elastic strain increment: $\Delta \boldsymbol{\epsilon}^e = \Delta \boldsymbol{\epsilon} - \Delta \boldsymbol{\epsilon}^p$
8	Compute stress increment: $\Delta \boldsymbol{\sigma} = \mathbf{C} * \Delta \boldsymbol{\epsilon}^e$
9	Compute incremental plastic work: $\Delta W^p = \frac{1}{2}(\boldsymbol{\sigma}_t + \boldsymbol{\sigma}_{t+1}) : \Delta \boldsymbol{\epsilon}^p$
10	Update variables: $\boldsymbol{\sigma}_{t+1} = \boldsymbol{\sigma}_t + \Delta \boldsymbol{\sigma};$ $p_{t+1} = p_t + \Delta p;$ $W_{t+1}^p = W_t^p + \Delta W^p$

Appendix B

Chemical kinetics and diffusion

B.1 Reaction and diffusion equations

$$\frac{d[O_2]}{dt} = D_{O_2} \frac{\partial^2 [O_2]}{\partial x^2} - k_2 [O_2] [P^\circ] + k_{6a} [PO_2^\circ]^2 \quad (\text{B.1})$$

$$\frac{d[DOC]}{dt} = D_{DOC} \frac{\partial^2 [DOC]}{\partial x^2} - k_{1D} [DOC] [PE] - n_{AO} k_{1s} [DOC] [AO] - k_7 [DOC] [P^\circ] \quad (\text{B.2})$$

$$\frac{d[AO]}{dt} = D_{AO} \frac{\partial^2 [AO]}{\partial x^2} - n_{AO} k_{1s} [DOC] [AO] - n_{AO} k_{s1} [PO_2^\circ] [AO] \quad (\text{B.3})$$

$$\begin{aligned} \frac{d[PO_2^\circ]}{dt} = & k_{1b} [POOH]^2 + k_2 [O_2] [P^\circ] - k_3 [PE] [PO_2^\circ] - k_5 [P] [PO_2^\circ] - 2k_{6a} [PO_2^\circ]^2 \\ & - n_{AO} k_{s1} [PO_2^\circ] [AO] \quad (\text{B.4}) \end{aligned}$$

$$\begin{aligned} \frac{d[P^\circ]}{dt} = & 2k_{1u}[POOH] + k_{1b}[POOH]^2 + k_{1d}[DOC][PE] - k_2[O_2][P^\circ] + k_3[PE][PO_2^\circ] - \\ & 2k_4[P^\circ]^2 - k_5[P^\circ][PO_2^\circ] + 2k_{6d}[Q] - k_7[P^\circ][DOC] \quad (B.5) \end{aligned}$$

$$\frac{d[POOH]}{dt} = -k_{1u}[POOH] - 2k_{1b}[POOH]^2 + k_3[PE][PO_2^\circ] + (1 - \gamma_5)k_5[P^\circ][PO_2^\circ] \quad (B.6)$$

$$\frac{d[Q]}{dt} = k_{6a}[PO_2^\circ]^2 - (k_{6b} + k_{6c} + k_{6d})[Q] \quad (B.7)$$

Q = caged pair of PO° radicals

$$\begin{aligned} \frac{d[PE]}{dt} = & -(2 + \gamma_{1s})k_{1u}[POOH] - (1 + \gamma_{1s})k_{1b}[POOH]^2 - k_{1d}[DOC][PE] - \\ & k_3[PE][PO_2^\circ] + 2\gamma_4k_4[P^\circ]^2 + (3\gamma_5 - 1)k_5[P^\circ][PO_2^\circ] + 2k_{6b}[Q] - 2(1 + \gamma_{1s})k_{6d}[Q] \quad (B.8) \end{aligned}$$

$$\frac{d[CO]}{dt} = \gamma_{1CO}k_{1u}[POOH] + \gamma_{1CO}k_{1b}[POOH]^2 + k_{6c}[Q] + 2\gamma_{1CO}k_{6d}[Q] \quad (B.9)$$

$$\frac{d[PCl]}{dt} = k_7[P^\circ][DOC] \quad (B.10)$$

$$\frac{d[\bar{s}]}{dt} = \gamma_{1s}k_{1u}[POOH] + \gamma_{1s}k_{1b}[POOH]^2 + 2\gamma_{1s}k_{6d}[Q] \quad (B.11)$$

$$\frac{d[\bar{x}]}{dt} = \gamma_4k_4[P^\circ]^2 + \gamma_5k_5[P^\circ][PO_2^\circ] + k_{6b}[Q] \quad (B.12)$$

$$\frac{1}{M_2} - \frac{1}{M_{W0}} = \frac{\bar{s}}{2} - 2\bar{x} \quad (\text{B.13})$$

B.2 Matlab simulation code

Attached is a sample Matlab program to solve the chemical reaction and diffusion equations developed by Colin et al. The embedded Matlab partial differential equation solver PDEPE is utilized.

```
1 %Colin_pdepe
   %This program solves the Colin diffusion reaction problem using
   %PDEPE
3 %%
   %Define the Left and Right bound for distance in mm
5 xR=4.2;
   xL=0;
7 %Define the total time for simulation in seconds
   Total_time=2.07e8;
9 Total_time_inc=Total_time/1e6+1;
   %%
11 m=0;
   x= linspace(xL*1e-3,xR*1e-3,(xR-xL)*10+1);
13 t= linspace(0, Total_time, Total_time_inc);
   opt = odeset('RelTol',1e-3, 'AbsTol',1e-15);
15
   sol=pdepe(m, @colinfun, @colinic_0, @colinbc, x, t, opt);
17
   u1=sol(:, :, 1);
19 u2=sol(:, :, 2);
   u3=sol(:, :, 3);
21 u4=sol(:, :, 4);
   u5=sol(:, :, 5);
23 u6=sol(:, :, 6);
```



```

u7=sol (: , : , 7) ;
25 u8=sol (: , : , 8) ;
u9=sol (: , : , 9) ;
27 u10=sol (: , : , 10) ;
u11=sol (: , : , 11) ;
29 u12=sol (: , : , 12) ;

31 Mw0=150.*ones (length (x) , 1) ;

33 %%
%Export data
35 xlsfilename='Sim_results_sum1.xlsx' ;

37 result_sum=[x' , u1 (end , : ) ' , u2 (end , : ) ' , u3 (end , : ) ' , ...
u4 (end , : ) ' , u5 (end , : ) ' , u6 (end , : ) ' , ...
39 u7 (end , : ) ' , u8 (end , : ) ' , u9 (end , : ) ' , ...
u10 (end , : ) ' , u11 (end , : ) ' , u12 (end , : ) ' , Mw] ;

41
xlswrite (xlsfilename , result_sum , '2.07e8sec' , 'A1' )
43
%%
45 %Generate molecular weight as a function of time for each
location
% A single matrix will be used to store the molecular weight
history
47 % for each 'x' location. Dimension of this matrix is:
% length (t) * length (x)
49 % For each location , the molecular weight history will be stored
% in a column.

```

```

51 Mw_matrix=zeros(length(t),length(x));
53
55 for i=1:length(x)
57     for j=1:length(t)
59         Mw_matrix(j,i)=1/(u11(j,i)/2-2*u12(j,i)+1/Mw0(i));
61     end
end
xlsfilename='Sim_results_Mwhistory1.xlsx';
xlswrite(xlsfilename,round(Mw_matrix),'iteration_0','A1')

```

```

function [ c,f,s ] = colinfun( x,t,u,DuDx )
2 %The yield parameters, from Colin I
gamma_5= 1.08e-2;
4 gamma_1s= 1;
gamma_4=0.5;
6 gamma_1CO=0.7;

8 %%Specification of rate constants. Numbers are calculated from
Colin Audouin
%%2009 I, at 20C.
10 k1u=9.05e-13;
k1b=5.46e-10;
12 k1d=2.7e-5;
k2=1e8;
14 k3=1.47e-3;
k4=8e11;
16 k5=1.33e11;

```

```

k6a=2.72e5;
18 k6b=2e6;
k6c=1.54e5;
20 k6d=3.81e6;
k7=1.15e6;
22 %
% %Specification of diffusion coefficients calculated based on
% Colin II @ 20C
24 D_O2=2.49e-11;
D_DOC=2e-11;
26 D_AH=2.2e-16;
D_PO2=1e-30;
28 D_P=1e-30;
D_POOH=1e-30;
30 D_POPO=1e-30;
D_PH=1e-30;
32 D_CO=1e-30;
D_PCl=1e-30;
34 D_s=1e-30;
D_xx=1e-30;
36 %
% %Misc parameters
38 nah=4; %functionality of phenolic antioxidant
ks1=1.67; % at 20C
40 k1s=5e-2; % at 20C
%%
42 c=[1; 1; 1; 1; 1; 1; 1; 1; 1; 1; 1; 1];
f=[D_O2;D_DOC;D_AH;D_PO2;D_P;D_POOH;D_POPO;D_PH;D_CO;D_PCl;D_s;
D_xx].*DuDx; %

```

```

44 s=[-k2*u(1).*u(5)+k6a*u(4).^2; ...
    -k1d*u(2).*u(8)-nah*k1s*u(2).*u(3)-k7*u(2).*u(5);...
46 -nah*k1s*u(2).*u(3)-nah*ks1*u(4).*u(3);...
    k1b*u(6).^2+k2*u(1).*u(5)-k3*u(8).*u(4)-k5*u(5).*u(4)-2*k6a*u
    (4).^2-nah*ks1*u(4).*u(3); ...
48 2*k1u*u(6)+k1b*u(6).^2+k1d*u(2).*u(8)-k2*u(1).*u(5)+k3*u(8).*u
    (4)-2*k4*u(5).^2-k5*u(5).*u(4)+2*k6d*u(7)-k7*u(5).*u(2);
    ...
    -k1u*u(6)-2*k1b*u(6).^2+k3*u(8).*u(4)+(1-gamma_5)*k5*u(5).*u
    (4); ...
50 k6a*u(4).^2-(k6b+k6c+k6d)*u(7); ...
    -(2+gamma_1s)*k1u*u(6)-(1+gamma_1s)*k1b*u(6).^2-k1d*u(2).*u(8)
    -k3*u(8).*u(4)+2*gamma_4*k4*u(5).^2+(3*gamma_5-1)*k5*u(5).*
    u(4)+2*k6b*u(7)-2*(1+gamma_1s)*k6d*u(7); ...
52 gamma_1CO*k1u*u(6)+gamma_1CO*k1b*u(6).^2+k6c*u(7)+2*gamma_1CO*
    k6d*u(7); ...
    k7*u(5).*u(2); ...
54 gamma_1s*k1u*u(6)+gamma_1s*k1b*u(6).^2+2*gamma_1s*k6d*u(7);
    ...
    gamma_4*k4*u(5).^2+gamma_5*k5*u(5).*u(4)+k6b*u(7)];
56 end

```

```

1 function [pl, ql, pr, qr] = colinbc(xl, ul, xr, ur, t)
3 pl=[ul(1)-3.8e-4; ...
    ul(2)-2.25e-6; ...
5    0;0;0;0;0;0;0;0;0;0;0];
7 ql=[0;0;1;1;1;1;1;1;1;1;1;1];

```

```

9 pr = [0;0;0;0;0;0;0;0;0;0;0;0;0];
  qr = [1;1;1;1;1;1;1;1;1;1;1;1;1];
11
end

```

```

1 function [ u0 ] = colinic( x )
  %%
3 %Compile the initial condition when the simulation restarts from
  the end
  %of last iteration. The initial condition values have to be the
  same
5 %as that from the end of last iteration

7 %%
  %Initial condition setup for FIRST iteration
9 IC1=3.8e-4.*ones(1,length(x)); %[O2] 3.8e-4
  IC2=2.25e-6.*ones(1,length(x)); %2.25e-6 for 0.15ppm of [DOC] at
  20C
11 IC3=1.8e-3.*ones(1,length(x)); % [AH]
  IC4=1e-12.*ones(1,length(x)); %artificial initial value
13 IC5=1e-12.*ones(1,length(x)); %artificial initial value
  IC6=1e-2.*ones(1,length(x)); %[POOH]
15 IC7=1e-12.*ones(1,length(x)); %artificial initial value
  IC8=60.*ones(1,length(x));
17 IC9=1e-12.*ones(1,length(x)); %artificial initial value
  IC10=1e-12.*ones(1,length(x)); %artificial initial value
19 IC11=1e-12.*ones(1,length(x)); %artificial initial value
  IC12=1e-12.*ones(1,length(x)); %artificial initial value

```

21

%%

23

u0=[IC1; ...

IC2; ...

25

IC3; ...

IC4; ...

27

IC5; ...

IC6; ...

29

IC7; ...

IC8; ...

31

IC9; ...

IC10; ...

33

IC11; ...

IC12];

35

end